

## A Polar Low over the Japan Sea on 21 January 1997. Part II: A Numerical Study

WATARU YANASE

*Ocean Research Institute, University of Tokyo, Minamidai, Nakano, Tokyo, Japan*

GANG FU

*Department of Marine Meteorology, Ocean University of China, Quindao, China*

HIROSHI NIINO

*Ocean Research Institute, University of Tokyo, Minamidai, Nakano, Tokyo, Japan*

TERUYUKI KATO

*Meteorological Research Institute, Tsukuba, Japan*

(Manuscript received 13 December 2002, in final form 19 December 2003)

### ABSTRACT

A remarkable isolated polar low observed over the Japan Sea on 21 January 1997 is studied by numerical simulations using a 20-km-mesh regional primitive equation model [Regional Spectral Model (RSM) of the Japan Meteorological Agency] and a 5-km-mesh nonhydrostatic mesoscale model [Meteorological Research Institute Nonhydrostatic Model (MRI-NHM)] and by sensitivity experiments using the MRI-NHM.

The 24-h integration of RSM starting from 0000 UTC 21 January reproduces quite well the polar low's movement and development, including the initial wrapping of the west part of an east–west-oriented vorticity zone. The vorticity budget analysis indicates that the stretching term plays a dominant role in the polar low development.

The simulation by MRI-NHM reproduces surprisingly well the wrapping of the western part of the east–west-oriented vorticity zone associated with a cloud band, the spiral-shaped cloud pattern, and the “eye” structure near the vortex center. The wind speed and resulting sea surface heat fluxes of the simulated polar low exhibited a significant deviation from axisymmetry. The eye, almost free of cloud, was relatively dry and was associated with a strong downdraft and a warm core. A thermodynamic budget analysis indicates that the warm core is mainly caused by the adiabatic warming due to the downdraft.

Two types of sensitivity experiments using a 6-km-mesh MRI-NHM are performed: In the first type, the physical processes such as condensational heating and/or surface heat fluxes are switched on–off throughout the whole integration time of 24 h, as in the past sensitivity studies. In the second type, on the other hand, both condensational heating and surface heat fluxes are incorporated up to a certain time, but then one or all of them are switched on–off for the following 1 h. This minimizes the deformation of the environment of the vortex and is suitable for studying the direct effect of the physical processes on the vortex development.

The results of the sensitivity experiments show that the rapid development of the present polar low is principally caused by the condensational heating. The surface heat fluxes, on the other hand, are important for maintaining the environment that supports the vortex development; that is, the absence of the surface heat fluxes stabilizes the stratification in the boundary layer so that the vortex development is severely suppressed.

### 1. Introduction

Polar lows have received considerable attention in the literature in the past decades. Among oceans where polar lows frequently occur, the Japan Sea is located at the lowest latitude. Moreover, since the Japan Sea is

almost surrounded by the Eurasian continent and the Japanese islands, it is thought to be one of the most suitable areas to study polar lows: Upstream of the Japan Sea, a large number of upper-air observation stations are spread over the continent. Downstream, when polar lows make landfall on the Japanese islands, more detailed observational data can be obtained from the radar networks and the Automated Meteorological Data Acquisition System (AMeDAS).

During 20–21 January 1997, a remarkable isolated polar low occurred over the Japan Sea. An observational

---

*Corresponding author address:* Wataru Yanase, Dynamic Marine Meteorology Group, Dept. of Physical Oceanography, Ocean Research Institute, University of Tokyo, 1-15-1, Minamidai, Nakano 164-8639, Tokyo, Japan.  
E-mail: yanase@ori.u-tokyo.ac.jp

study of this polar low case is described in Part I of this paper (Fu et al. 2004, hereafter referred to as Part I). Using almost all available observational data, including the *Geostationary Meteorological Satellite-5 (GMS-5)* and the National Oceanic and Atmospheric Administration *NOAA-14* satellite as well as Sapporo and Niigata radar data, Part I documented the detailed evolutionary process of this polar low and the environmental condition that led to its generation. When the polar low was at its mature stage, a typical spiral-shaped cloud pattern and a clear “eye” structure were observed from the satellite and radar images. Also, a warm core structure associated with the polar low was found at the lower level.

Although Part I revealed a number of interesting aspects of the polar low, its detailed structure, dynamics, and development mechanism remain largely unclarified. In Part II, a numerical study on this polar low is conducted to explore these subjects. The numerical models used for this study are a 20-km-mesh Regional Spectral Model (RSM; Nakamura 1995) of the Japan Meteorological Agency (JMA) and a 5-km-mesh Meteorological Research Institute Nonhydrostatic Model (MRI-NHM; Saito 1998) that is nested into the RSM. The simulation of MRI-NHM will be shown to reproduce quite nicely the observed features of the polar low such as spiral-shaped bands and a clear eye structure, as well as its evolution and movement.

There have been only a limited number of numerical studies on polar lows using nonhydrostatic models. Bresch et al. (1997) made numerical simulation and sensitivity studies on a polar low over the Bering Sea using the fifth-generation Pennsylvania State University–National Center for Atmospheric Research Mesoscale Model (MM5). Most of the simulations were performed with a grid interval of 20 km and with Kain–Fritsch (1993) convective parameterization, in which the minimum convective cloud depth was reduced to 2 km. The simulated low resembled more closely an extratropical cyclone than a typical axisymmetric tropical cyclone. The results of a finer-resolution run (with 6.67-km grid interval) were nearly similar to those of the standard run. Pagowski and Moore (2001) used MM5 to study a polar low over the Labrador Sea and showed that the parameterization of the surface heat flux within the marginal ice zone affects the development of the polar low significantly. They also pointed out that a well-described model such as MM5 can have systematic errors of the surface fluxes during cold-air outbreaks. Yanase et al. (2002) reported preliminary results of a successful simulation of the present polar low case using a 2-km-mesh MRI-NHM. Detailed analysis of the simulation, however, is still in progress and has not been reported.

Generally speaking, there still remains a great deal of uncertainty concerning the development mechanism of polar lows because of their complex nature and difficulty in the observation. Since the first report on a polar low by Harley (1960), a number of development

mechanisms for polar lows have been suggested. At the early stage of the polar low study, polar lows were thought to develop by baroclinic instability (Harrold and Browning 1969; Mansfield 1974) or conditional instability of the second kind (CISK; Rasmussen 1979), which are important development mechanisms for extratropical and tropical cyclones, respectively. Using a linear model that includes both baroclinic instability and CISK, Sardie and Warner (1983) revealed that these two instabilities operate with different importance between a polar low over the Pacific Ocean and one over the Atlantic Ocean.

Recent suggestions of nonlinear mechanisms such as the wind-induced surface heat exchange (WISHE; Emanuel and Rotunno 1989) and the influence of an upper-level mobile disturbance (Montgomery and Farrell 1992) have made the interpretation of the polar low development even more complicated. On the other hand, advances in computer technology and mesoscale numerical models have enabled realistic simulations of a polar low (e.g., Yanase et al. 2002). To investigate the nonlinear development of a polar low, in particular, a numerical sensitivity experiment in which a certain physical process is artificially removed to examine its effect on the development seems to be a promising tool. Using a sensitivity experiment, Sardie and Warner (1985) revealed that surface heat flux is important for the polar low development over the Atlantic Ocean, whereas it is not for that over the Pacific Ocean. Thus the impact of various physical processes on polar low development can be different from area to area (e.g., Albright and Reed 1995; Bresch et al. 1997), which seems to reflect the difference of the development mechanisms in different areas. In order to examine the development mechanism of the polar low studied in Part I, we perform sensitivity experiments. It is also of interest to examine similarities and differences in development mechanisms between the polar low over the Japan Sea and that in other areas.

The commonly performed sensitivity experiments mentioned above, however, have one serious problem: an absence of a certain physical process for a long time (say, a day) affects not only the vortex itself but also the environment in which the vortex develops. Thus, it is often difficult to judge whether a certain physical process affects the vortex directly or indirectly through modification of its environment. For this reason, we have attempted a new type of sensitivity experiment in which the deformation of the environment is kept as small as possible. Based on the result of this experiment, we will discuss which physical process is directly important for the polar low development.

This paper is organized as follows: Section 2 presents the simulation results of RSM. These results are used to provide the environmental flow field in which MRI-NHM is to be nested. A rough comparison with the observation and a vorticity budget analysis around the polar low is also made. In section 3, we examine the

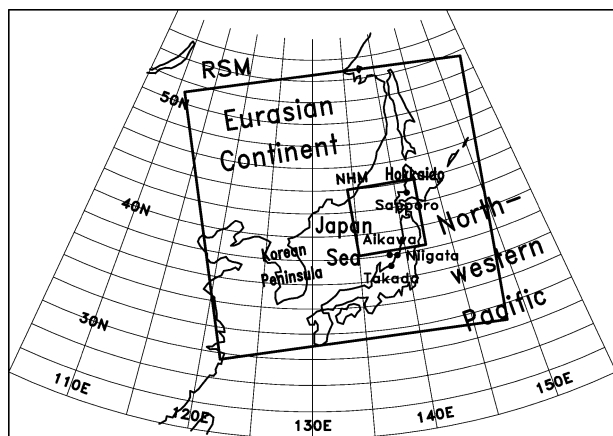


FIG. 1. Geographic map of east Asia and the northwestern Pacific. The large square shows the calculation domain for the RSM simulation, while the small one shows that for the MRI-NHM simulation.

detailed structure of the polar low based on the simulation results of the 5-km-mesh MRI-NHM. In section 4, sensitivity experiments are performed to study the development mechanism of the polar low. The results are discussed in section 5 and summarized in section 6.

## 2. Numerical simulation with RSM

### a. Model description

RSM has been the current operational regional weather prediction model of JMA since March 1996 (Nakamura 1995). Although the original operational model covers a somewhat wider area of east Asia, the present calculation domain is limited to the region shown in Fig. 1 because of the limitation of the computer resources. The specification of RSM used in the present study is summarized in Table 1. It is a primitive equation

model and has 36 levels in a  $\sigma$ -pressure hybrid coordinate system. In the horizontal direction, it uses a spectral representation and has a grid-equivalent resolution of 20 km at 30°N (60°N) on a Lambert projection plane. For convective parameterizations, a prognostic Arakawa-Schubert scheme together with the moist convection adjustment scheme for the middle-level convection is used. The 24-h simulation starting from the regional objective analysis (RANAL) data of JMA at 0000 UTC 21 January 1997 is performed.<sup>1</sup>

### b. Results

Figure 2 shows 2-hourly positions of the simulated polar low together with those observed by the satellite (see Fig. 11 of Part I), where the center of the simulated polar low has been determined from the surface pressure minimum. It is seen that the simulated center of the low always remains within 200 km of the observed center, which seems fairly satisfactory. The cause of the difference between the locations of simulated and observed low centers is not obvious, because the low center is merely a phase and can be affected by a number of factors such as environmental wind, surface fluxes, condensation heating, and so on. We note, however, that the initial location of the disturbance in the simulation is considerably to the east of the one observed from the satellite.

The simulated surface pressure distribution at 1400 UTC is also shown in Fig. 2. The diameter of the outermost closed isobar is about 100 km, and the central pressure is 996.5 hPa. The maximum vorticity is  $7.0 \times 10^{-4} \text{ s}^{-1}$  (not shown).

<sup>1</sup> Another simulation was performed from the RANAL data at 1200 UTC 20 January 1997. However, the polar low was not successfully reproduced in this simulation.

TABLE 1. Specification of RSM.

Categories	Specification in the present study
Basic equation	Primitive equations
Vertical coordinate	36 levels in $\sigma$ -pressure hybrid coordinate
Projection	Lambert projection
Advection scheme	Spectral scheme for limited-area models (Tatsumi 1986)
Horizontal resolution	20 km (at 30° and 60°N)
Horizontal grid points	129 × 129
Time integration	Semi-implicit for gravity waves
Turbulent closure	Level 2 (Mellor and Yamada 1974)
Precipitation scheme	Large-scale condensation Prognostic Arakawa-Schubert scheme Moist convective adjustment scheme for middle-level convection (Benwell and Bushby 1970; Gadd and Keers 1970)
Evaporation of raindrops	Included (Ogura and Takahashi 1971)
Parameterization of water loading	Included
Radiation	Long- and shortwave radiation (Sugi et al. 1990)
Surface layer	Louis scheme (Louis et al. 1981)
Lower boundary	Forecast using four-layer model
Upper boundary	Rigid wall at 0 hPa
Lateral boundary	Nesting within RANAL with relaxation (Davies 1976)
Numerical diffusion	Fourth-order linear damping

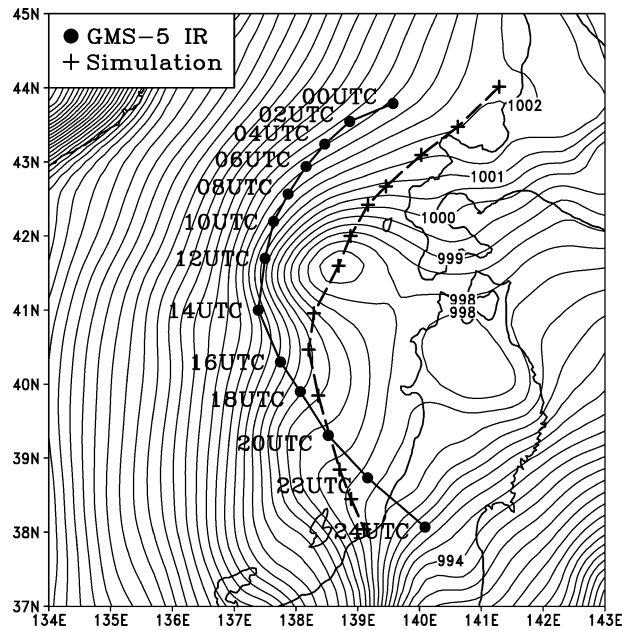


FIG. 2. The simulated surface pressure distribution at 1400 UTC 21 Jan 1997 by RSM. The isobars are drawn for each 0.5 hPa. Also shown are the tracks of the polar low centers simulated by RSM (indicated by cross symbol) and observed from the satellite (indicated by solid circle).

Since the detailed structure of the polar low is examined based upon the simulation using MRI-NHM, here we are only concerned with its vorticity dynamics. Figure 3 shows the time evolution of the maximum vorticity of the simulated polar low at the levels of 950, 925, 900, and 850 hPa. Also shown in the figure is the time evolution of the surface central pressure. The sharp increase of the vorticity and the decrease of the pressure from 0900 to 1400 UTC suggest that the polar low was at its developing stage during that period (cf. Fig. 11 of Part I). From 1400 to 1500 UTC the vorticity increased only slightly. The polar low reached its most mature stage at 1500 UTC when the vorticity attained its maximum value of  $9.5 \times 10^{-4} \text{ s}^{-1}$  and the pressure reached the minimum value of 996.3 hPa. After 1500 UTC, the polar low started to dissipate gradually.

In order to understand the vorticity dynamics associated with the polar low development, the contribution of each term in the vorticity equation to the time change rate of vorticity is examined. The vertical vorticity equation in an isobaric coordinate is written as

$$\frac{\partial \zeta}{\partial t} = -\mathbf{V}_h \cdot \nabla_h (\zeta + f) - \omega \frac{\partial \zeta}{\partial p} - (\zeta + f) \nabla_h \cdot \mathbf{V}_h - \mathbf{k} \cdot \left( \frac{\partial \mathbf{V}_h}{\partial p} \times \nabla_h \omega \right) + D_\zeta, \quad (1)$$

where the term in the left-hand side is the local time change rate of the vorticity. In the right-hand side, the first and second terms are the horizontal and vertical

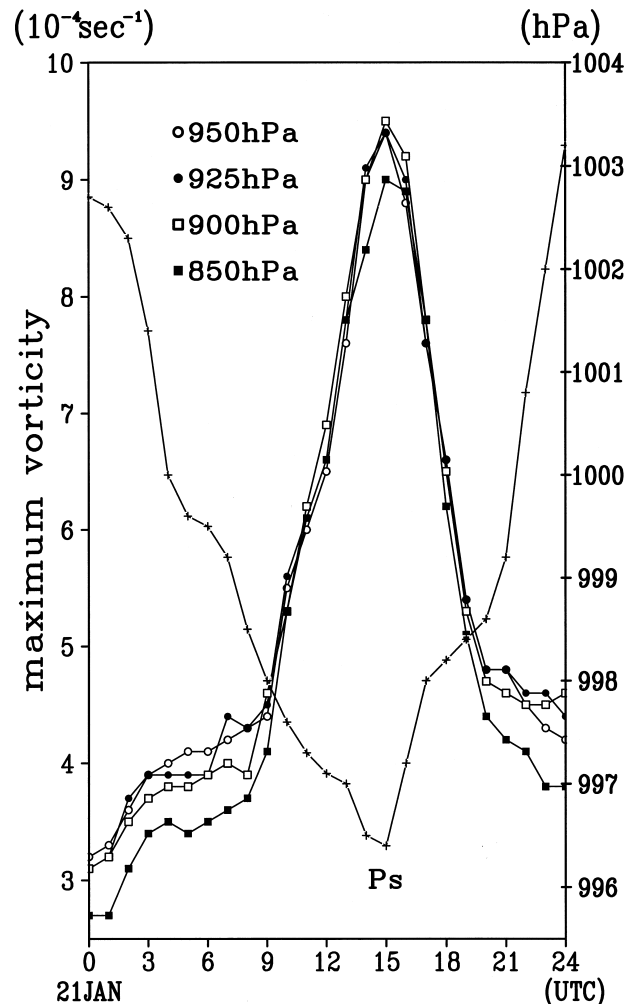


FIG. 3. The time evolution of the maximum vorticity ( $10^{-4} \text{ s}^{-1}$ ) at the levels of 950, 925, 900, and 850 hPa, and the surface central pressure of the polar low (hPa) simulated by RSM.

advectations of vorticity, respectively, the third term is the stretching, the fourth term the tilting, and the fifth term the frictional term.

The horizontal distributions of vorticity and stretching terms in Eq. (1) at  $t = 0700, 1100, 1500,$  and  $1900$  UTC at 900 hPa are presented in Figs. 4 and 5, respectively, and those of horizontal advection, vertical advection, and tilting terms at  $t = 1500$  UTC are shown in Fig. 6. The times  $t = 0700, 1100, 1500,$  and  $1900$  UTC correspond to initial, developing, mature, and dissipating stages in the simulation, respectively. Figures 5 and 6 show that the stretching and horizontal advection terms are the major contributors to the vorticity dynamics, and vertical advection and tilting terms are relatively minor. The horizontal advection term contributes mainly to shift the vorticity pattern toward the direction of the movement of the polar low and does not contribute to amplify the vorticity. Thus the stretching term plays the dominant role in the polar low development.

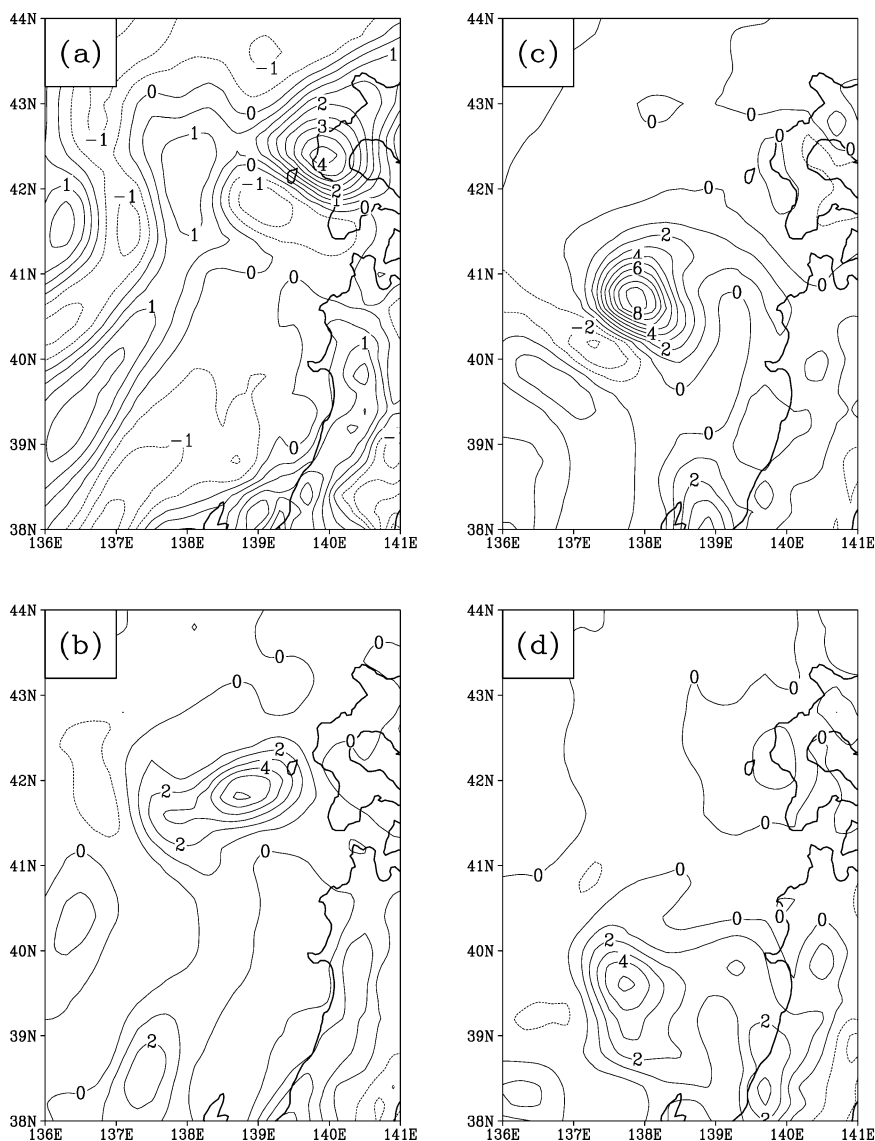


FIG. 4. The spatial distributions of the vorticity ( $10^{-4} \text{ s}^{-1}$ ) at 900 hPa simulated by RSM: (a)  $t = 0700$ , (b)  $t = 1100$ , (c)  $t = 1500$ , and (d)  $t = 1900$  UTC.

At 0700 UTC, the vorticity center is located near the southwestern coast of Hokkaido Island (Fig. 4a). The maximum vorticity at this initial stage is already about  $4.0 \times 10^{-4} \text{ s}^{-1}$  and is considerably larger than the planetary vorticity  $f \sim 1.0 \times 10^{-4} \text{ s}^{-1}$ . The Advanced Earth Observing System/National Aeronautics and Space Administration (NASA) Scatterometer (ADEOS/NSCAT) sea surface wind (Fig. 5 of Part I) also showed that the vertical vorticity associated with the cloud band was estimated to be about  $3.0 \times 10^{-4} \text{ s}^{-1}$ . Thus, it is considered that the vorticity dynamics may be essentially described in terms of the relative vorticity, and it does not much depend on the planetary vorticity throughout its lifetime. By 1100 UTC, the vorticity distribution is somewhat elongated to the east–west direction corresponding to the shear zone associated with the cloud

band (Fig. 5 of Part I). At 1500 UTC (Fig. 4c), during the mature stage, the maximum vorticity exceeds  $9.0 \times 10^{-4} \text{ s}^{-1}$ , and the vorticity contour lines become nearly concentric circles. A region of low vorticity intrudes from southwest to the east of the vortex. By 1900 UTC, the vorticity decreases to  $5.0 \times 10^{-4} \text{ s}^{-1}$  (Fig. 4d).

As was mentioned above, the stretching term is most dominant (Figs. 5 and 6). At 0700 UTC (Fig. 5a), the distribution of the stretching term is less significant yet. A region of mean positive stretching exists along the E–W-oriented cloud band. Its magnitude is about  $1.5 \times 10^{-4} \text{ s}^{-1} \text{ h}^{-1}$ , which explains the slow growth of vorticity at this time (cf. Fig. 3). During the next 4 h, however, a significant change occurs (Fig. 5b). At 1100 UTC, the distribution of the stretching term becomes very similar to that of the vorticity distribution in Fig.

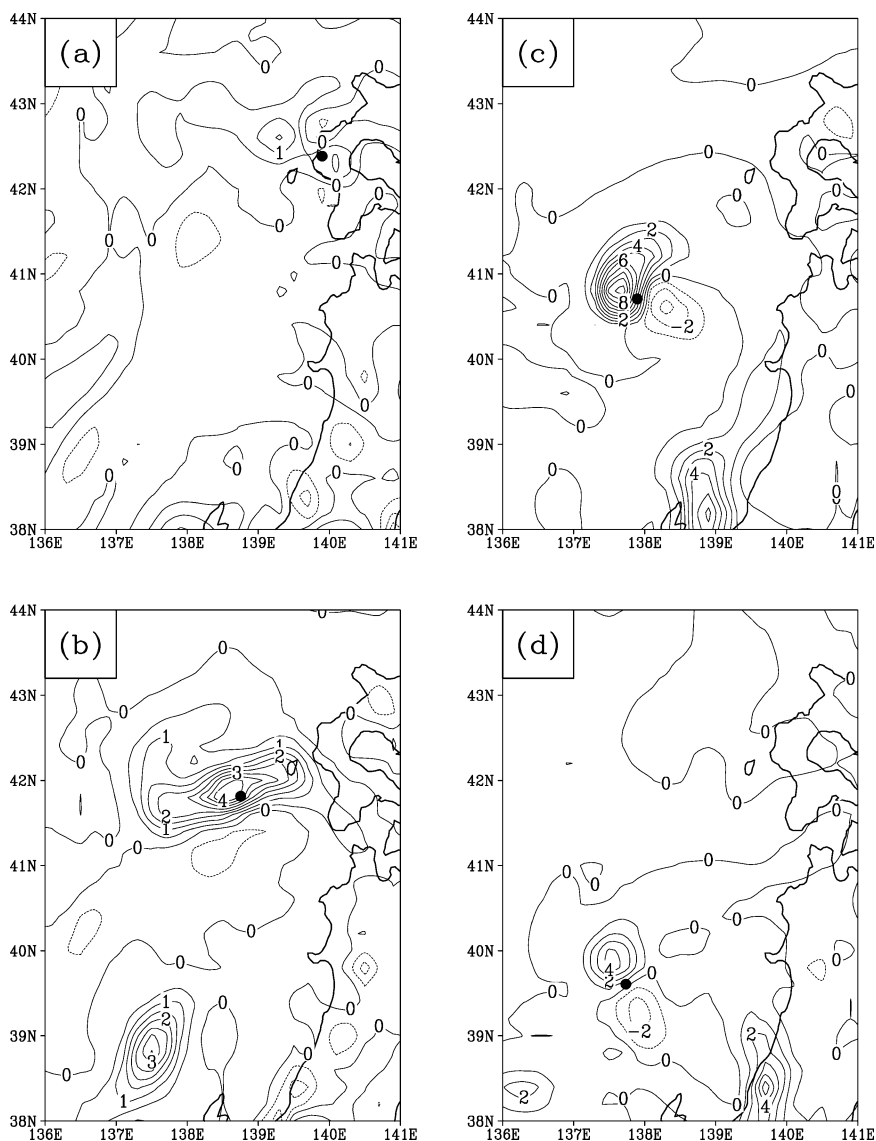


FIG. 5. Same as Fig. 4 except for the stretching term ( $10^{-4} \text{ s}^{-1} \text{ h}^{-1}$ ). The location of the maximum vorticity is indicated by solid circles.

4b. It is elongated in the east–west direction. Its magnitude reaches  $4.0 \times 10^{-4} \text{ s}^{-1} \text{ h}^{-1}$ . At 1500 UTC, the magnitude of the stretching term reaches  $9.0 \times 10^{-4} \text{ s}^{-1} \text{ h}^{-1}$  (Fig. 5c). Two interesting features are readily noted: First, this magnitude of the stretching term would double the vorticity within 1 h. Since the stretching term is much larger than the other terms, this means that there must be some dissipation mechanism to counteract the amplification effect of the stretching term. Second, unlike the distribution of the vorticity, that of the stretching term is not axisymmetric. At 1900 UTC (Fig. 5d), the distribution of the stretching term looks like a doublet rather than a concentric circle. The peak of the stretching term does not coincide with the peak of the vorticity, indicating that a further increase of vorticity is not possible.

The horizontal advection term is the second largest (Fig. 6a). Its distribution remains nearly similar from 0700 to 1500 UTC (not shown) in the sense that it is positive to the south of the vortex and negative to the north. This pattern simply represents the fact that the vortex is advected by the northerly wind. Thus, the horizontal advection term contributes to translate the distribution of the vorticity but does not contribute much to intensify the vortex. The vertical advection (Fig. 6b) and tilting terms (Fig. 6c) always remain much smaller than the stretching term.

### 3. Numerical simulation with MRI-NHM

As we have seen in the previous section, the gross features of this polar low have been reasonably repro-

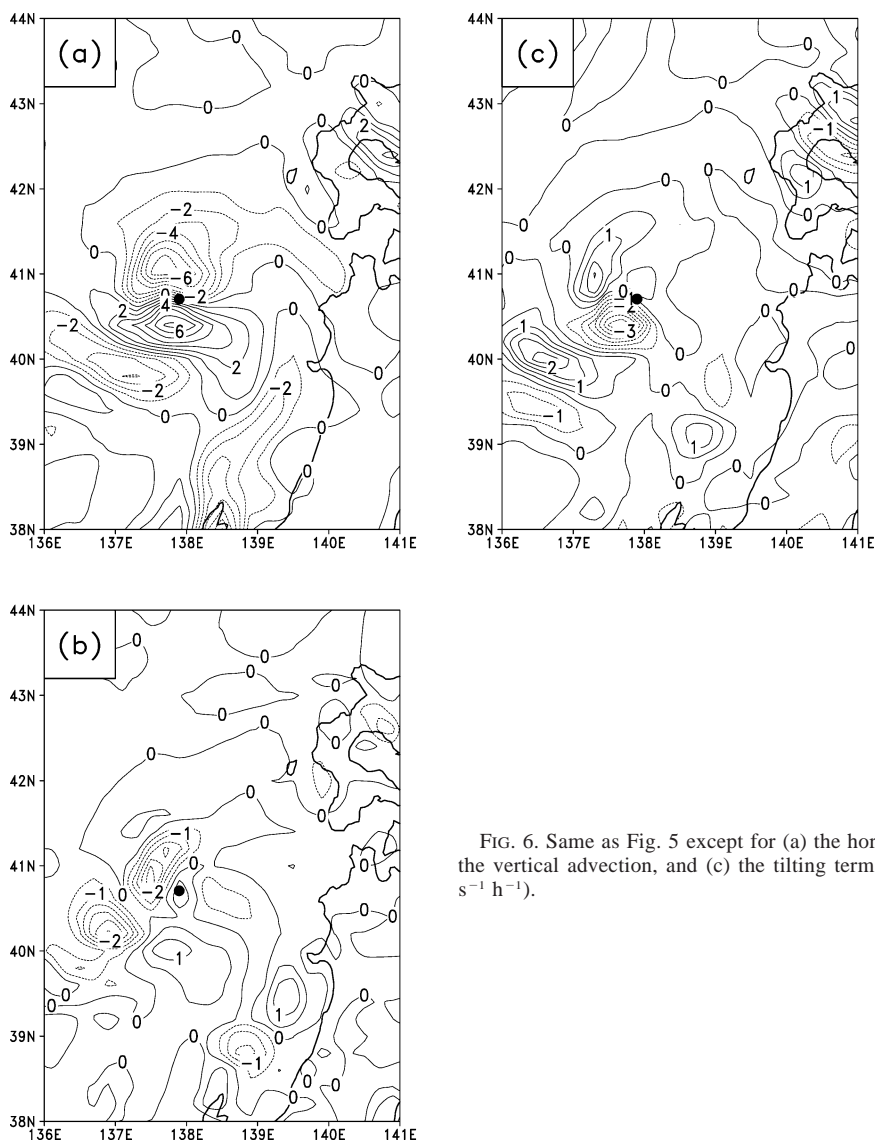


FIG. 6. Same as Fig. 5 except for (a) the horizontal advection, (b) the vertical advection, and (c) the tilting terms at 1500 UTC ( $10^{-4} \text{ s}^{-1} \text{ h}^{-1}$ ).

duced by RSM. In order to examine the detailed structure of the polar low, a further numerical simulation with MRI-NHM nested within RSM was performed.

*a. Model description*

MRI-NHM is a three-dimensional nonhydrostatic model developed by the Forecast Research Department of the Meteorological Research Institute, Japan (Ikawa and Saito 1991; Saito and Kato 1996), and modified so that it can be nested within an outer coarse-mesh model (Saito 1994). The main features of MRI-NHM are summarized in Table 2.

The model is formulated in terms of the fully compressible Navier–Stokes equations with a map factor in the terrain-following coordinate system. In the model, the ground temperature is predicted (Kato 1996), while the sea surface temperature is fixed to a daily analysis

supplied by JMA. A cold-rain scheme in which six variables of mixing ratios of water vapor  $q_w$ , cloud water  $q_c$ , rain  $q_r$ , cloud ice  $q_i$ , snow  $q_s$ , and graupel  $q_g$  are predicted is used, and a box-Lagrangian raindrop scheme (Kato 1995) is employed.

In the present study, the calculation domain was chosen to cover the path of the polar low center at its initial and developing stages (see Fig. 1). It has  $122 \times 122$  horizontal grid points. The horizontal grid sizes of  $\Delta x = \Delta y = 5 \text{ km}$  are used. The number of the vertical grid points is 38, where the grid interval increases from 40 m near the surface to 1090 m near the top of the calculation domain, which is at 20.36 km above ground level (AGL). The time step of integration  $\Delta t = 10 \text{ s}$  is used. The initial and boundary conditions are provided from the output of the RSM simulation results. The horizontal velocity components, potential temperature, mixing ratio of water vapor, surface pressure, and sur-

TABLE 2. Specification of the MRI-NHM.

Categories	Specification in the present study
Basic equations	Fully compressible nonhydrostatic Navier–Stokes equations with a map factor (Saito 1997)
Vertical coordinate	Terrain-following (Gal-Chen and Somerville 1977); 38 levels (fine resolution in the boundary layer)
Projection	North polar stereographic projection
Advection scheme	Arakawa C grid (Ikawa and Saito 1991) Second-order flux form Box-Lagrangian raindrop scheme (Kato 1995)
Horizontal resolution	5 km (at 32.5°N)
Time integration	Both vertically and horizontally implicit for sound waves ( $\Delta t = 10$ s)
Turbulent closure	Deardorff level 2.5 (Saito 1993)
Precipitation scheme	Cold-rain scheme (predicting $q_v, q_c, q_r, q_i, q_s, q_g$ )
Radiation	Long- and shortwave radiation
Surface layer	Bulk method based on Monin–Obukhov similarity [over land: Sommeria (1976); over sea: Kondo (1975)]
Lower boundary	Forecast using four-layer model (Kato 1996)
Upper boundary	Rigid lid; thermally insulated Rayleigh friction layer
Lateral boundary	Radiative nesting boundary condition (Saito 1994); nesting within RSM (Saito 1998)
Numerical diffusion	Fourth-order linear damping

face temperature are used for the nesting. No relaxation is imposed on the variables except for the topography, which has a transition zone of five grid points. The boundary values for the MRI-NHM are interpolated from gridpoint values of the RSM near the boundaries; for example, the vertical gridpoint values at the 38-layer  $z^*$ -coordinate system of MRI-NHM are interpolated from those at the 36-layer  $\sigma$ -pressure hybrid coordinate system of RSM. The initial time is 0000 UTC 21 January 1997, and the period of the integration is 24 h.<sup>2</sup>

### b. Results

#### 1) OVERVIEW

Figure 7 shows the simulated vorticity field and horizontal wind vector at the lowest level ( $z = 20$  m) from 1300 to 1800 UTC 21 January 1997. At 1300 UTC, an E–W-oriented high-vorticity region is clearly seen around the latitude line 41.5°N. This high-vorticity region corresponds to a shear zone between northeasterly wind in the northern side and north-northwesterly wind in the southern side. Such features correspond well to the observed structure of the E–W-oriented cloud band (see Fig. 5 of Part I) except that the intensification of the polar low is somewhat delayed in the simulation. The maximum vorticity that seems to correspond to the initial polar low is located near 138.8°E. It is interesting to note that another vorticity peak, similar to the third vortex in Figs. 4l–n in Part I, existed around 139.4°E. In the region of northeasterly wind north of the shear zone, several stripe patterns of vorticity whose axes are oriented to the NE–SW direction are seen. They cor-

respond to the cloud streets found in the satellite picture (see Fig. 6 of Part I).

As was mentioned above, the strong E–W-oriented horizontal shear zone exists along the latitudinal line of 41.5°N at 1300 UTC (Fig. 7a). The examination of the N–S cross section of this shear zone shows that the horizontal shear of the zonal flow  $U$  mainly concentrates on the zone 41.4°–41.6°N below 1200 m (not shown), and its maximum magnitude reaches  $1.8 \times 10^{-3} \text{ s}^{-1}$ . According to the linear barotropic instability theory (Gill 1982, p. 567), the fastest growing mode of a barotropically unstable disturbance has a growth rate  $\sigma_{\max} \approx 0.2dU/dy$  at the wavelength  $\lambda_{\max} \approx 16L$ , where  $L \sim 13$  km is the half-width of the shear zone. It is estimated that  $\sigma_{\max}$  is  $2.3 \times 10^{-4} \text{ s}^{-1}$ , which corresponds to an  $e$ -folding time of 1.2 h, and  $\lambda_{\max}$  is about 200 km, which is in good agreement with the initial size of the vortex (see Fig. 4 of Part I). A similar analysis for the linear baroclinic instability (Gill 1982, p. 557) indicated that the maximum growth rate,  $\sigma_{\max} \approx 0.31f/N \times dU/dz$ , occurs when the wavelength  $\lambda_{\max} \approx 7.8NH/f$ . Since the simulation results show that  $dU/dz \approx 6.81 \times 10^{-3} \text{ s}^{-1}$ , and  $N \sim 1.1 \times 10^{-2} \text{ s}^{-1}$ , it is estimated that  $\sigma_{\max} \sim 2.11 \times 10^{-5} \text{ s}^{-1}$ , which corresponds to an  $e$ -folding time of 13.2 h, and  $\lambda_{\max} \sim 500$  km. Thus, the vortices found in the shear zone (Figs. 4l–n of Part I; Fig. 7a) are likely to be caused by a barotropic instability.

As time elapses, the principal axis of the high-vorticity region has rotated anticlockwise as observed. The high-vorticity region gradually loses its approximate uniformity in the direction of the principal axis and is divided into high-vorticity cores (Fig. 7b). It is also noted that the eastern part of the high-vorticity region becomes weaker. The initial polar low moves southwestward while keeping its vorticity level (Figs. 7b,c). After 1600 UTC, the polar low changes its direction of movement southward and starts to develop rapidly. At

<sup>2</sup> Because of the limitation of our computer resources, the calculation domain of MRI-NHM has to be kept small. Accordingly, the polar low moved southward and went out of the domain after  $t = 2200$  UTC.

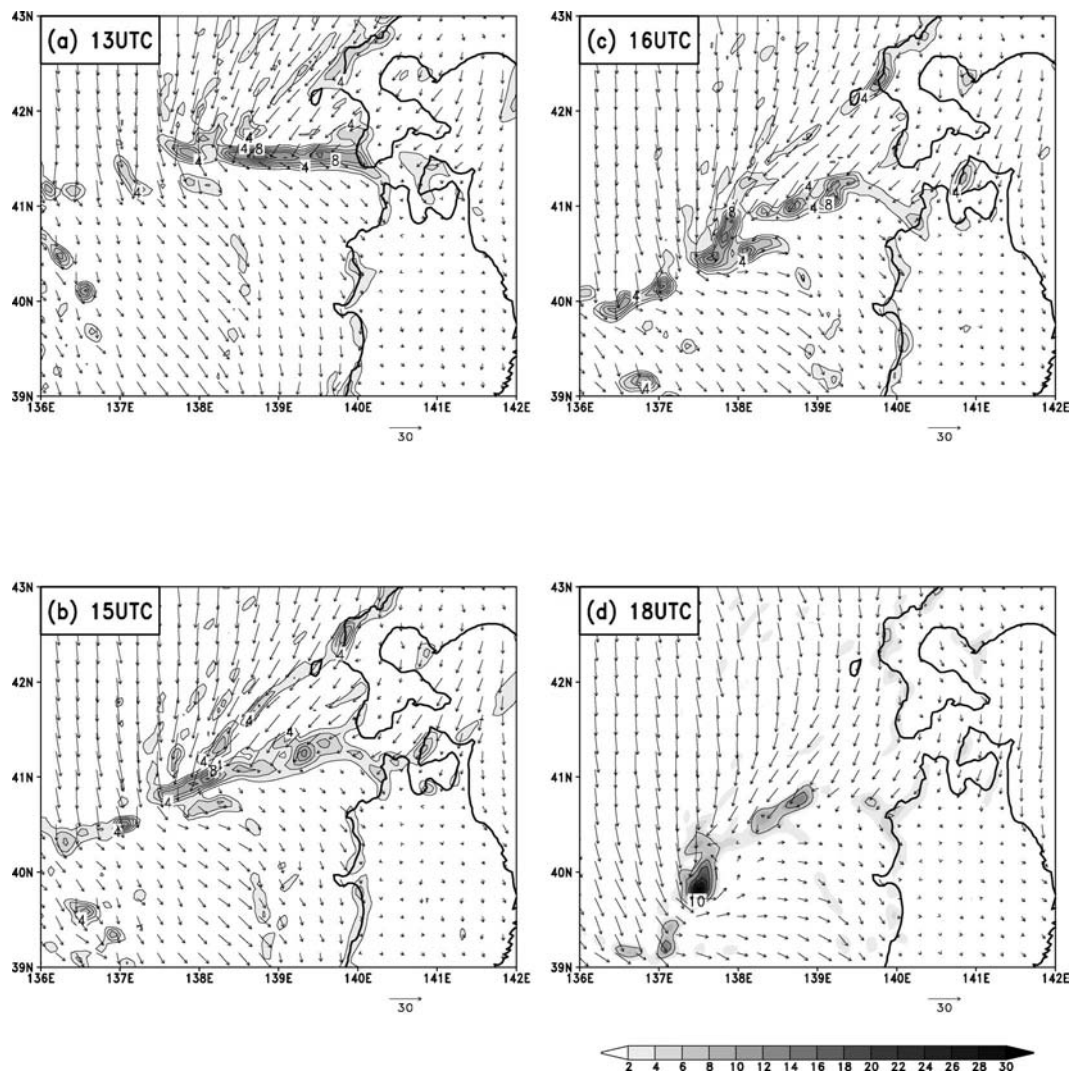


FIG. 7. The wind vector and vorticity field ( $10^{-4} \text{ s}^{-1}$ ) from 1300 to 1800 UTC 21 Jan 1997 simulated by MRI-NHM. The wrapping up of the western part of the vorticity band can be seen clearly: (a)  $t = 1300$ , (b)  $t = 1500$ , (c)  $t = 1600$ , and (d)  $t = 1800$  UTC.

1800 UTC, it attains the mature stage (Fig. 7d). The timing of the development of the polar low is somewhat delayed compared to the observation. Considering that the small-scale vortices, which appear to be caused by a barotropic instability and are difficult to predict deterministically, might play some role in the initial development of the polar low, we think that the simulation seems to be quite satisfactory. Accordingly, we examine the detailed structure of the mature polar low at 1800 UTC in the following.

## 2) STRUCTURE OF THE POLAR LOW

Figure 8a shows the horizontal distribution of vertically integrated total water particles per unit area at 1800 UTC, where total water particles refer to the sum of cloud water, cloud ice, rain, snow, and graupel. A spiral-

shaped cloud pattern that extends northeastward from the low center and a clear eye structure surrounded by the spiral-shaped cloud are reproduced in good agreement with the satellite observation. Yanase et al. (2002) succeeded in reproducing the present polar low by using a nonhydrostatic model with a horizontal grid interval of 2 km. However, a detailed analysis of the flow field has not been reported yet.

Figure 8b shows the horizontal distributions of the total surface heat flux (the sensible plus latent heat fluxes) together with the surface pressure. Generally speaking, the sensible heat flux is about 1.5 times as large as the latent heat flux. The total heat flux exhibits a remarkable east–west asymmetry as was also found by Yanase et al. (2002). In the western quadrant of the low, the total surface heat flux exceeds  $800 \text{ W m}^{-2}$ , while it is less than  $300 \text{ W m}^{-2}$  in the eastern side. This asym-

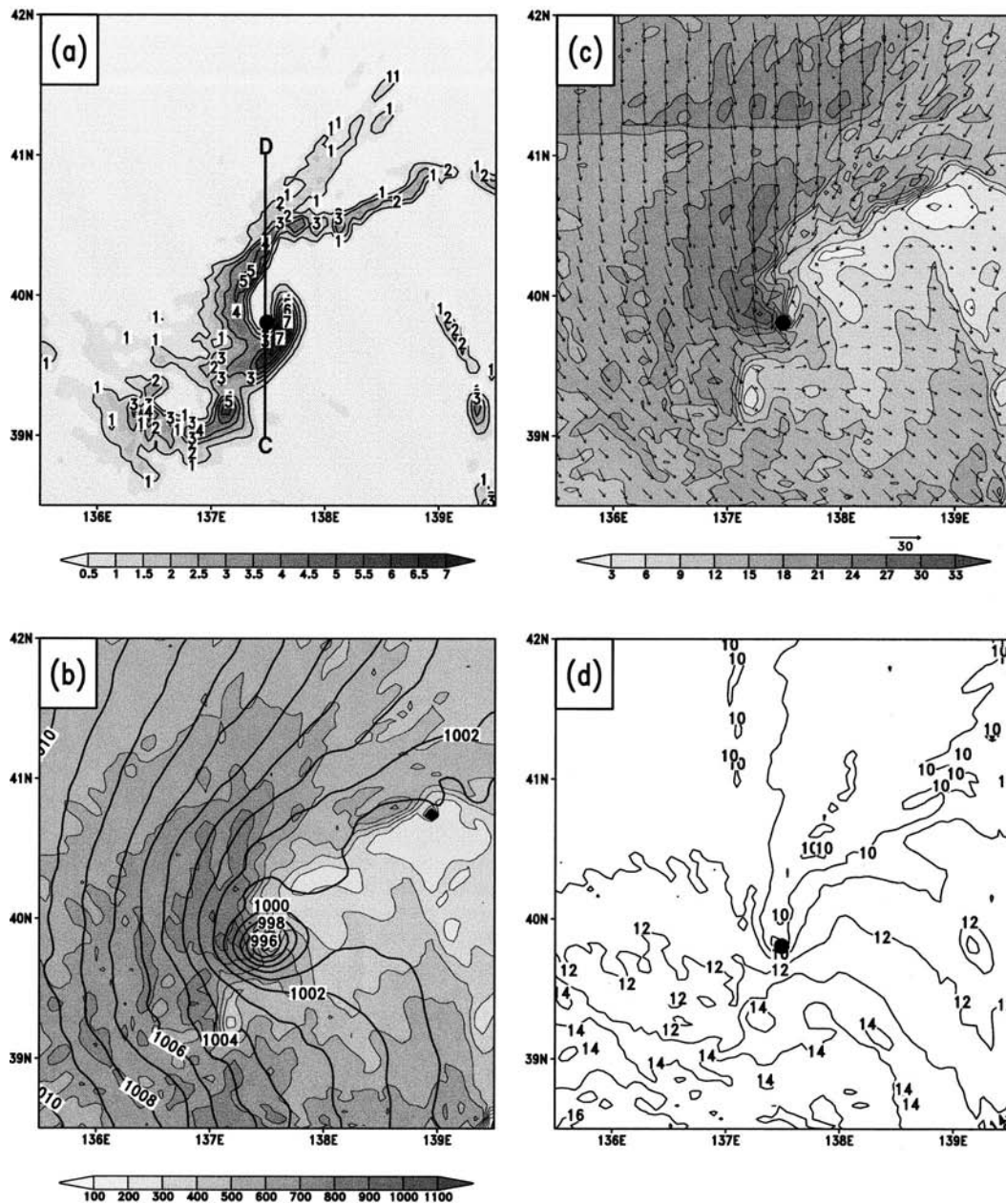


FIG. 8. Horizontal distributions of (a) vertically integrated total water particles (the sum of cloud water, cloud ice, rain, snow, and graupel) per unit area ( $\text{kg m}^{-2}$ ), (b) sum of sensible and latent surface heat fluxes (shaded;  $\text{W m}^{-2}$ ) and surface pressure (contour line; hPa), (c) surface wind speed (shaded;  $\text{m s}^{-1}$ ) and horizontal wind vector, and (d) the air-sea temperature difference ( $^{\circ}\text{C}$ ) at 1800 UTC 21 Jan 1997. The surface low center is indicated by a solid circle in (a) and (c).

metry in the total heat flux is mainly caused by the asymmetry of the wind speed. Figure 8c shows the horizontal wind vectors and the magnitude of the wind speed. It is seen that strong northerly wind with a maximum wind speed of  $30 \text{ m s}^{-1}$  prevails on the northwestern side of the low, while, on the eastern side, the magnitude of the wind speed is strikingly smaller than that of the western side. A strong convergence is seen near the spiral band and the surface low center. The air-

sea temperature difference defined by the difference between the SST and the air potential temperature at the lowest model level ( $z = 20 \text{ m}$ ), on the other hand, shows a north-south gradient rather than an east-west asymmetry (Fig. 8d). The smallest air-sea temperature difference near the low center reflects the existence of a warm core at its low level.

The large deviation from axisymmetry makes it difficult to examine if the WISHE instability mechanism

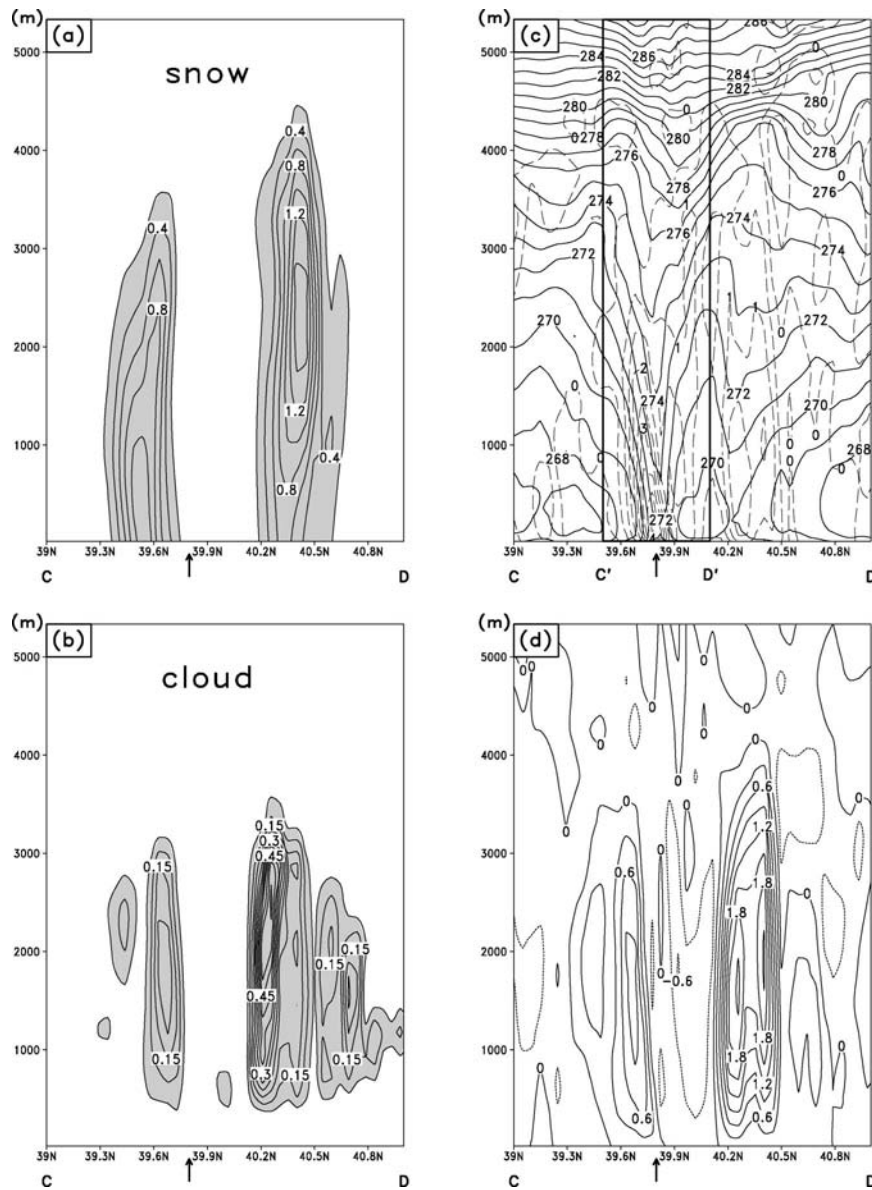


FIG. 9. Vertical cross section along the line CD in Fig. 8: (a) snow mixing ratio  $q_s$  ( $10^{-3}$  kg  $kg^{-1}$ ), (b) cloud mixing ratio  $q_c$  ( $10^{-3}$  kg  $kg^{-1}$ ), (c) potential temperature  $\theta$  (solid line; K) and vorticity (dashed line;  $10^{-3}$  s $^{-1}$ ), and (d) vertical velocity  $w$  (in m s $^{-1}$ ). The surface low center is indicated by the arrow. The interval between C' and D' in panel (c) is enlarged for detailed examination in Fig. 10.

(e.g., Emanuel 1986; Emanuel et al. 1994; Craig and Gray 1996; Gray and Craig 1998) is occurring in the simulated polar low. We have plotted contours of the equivalent potential temperature  $\theta_e$  and absolute angular momentum in four quadrants of the polar low (not shown). The results show that only on the western quadrant of the polar low is  $\theta_e$  nearly uniform along the surfaces of constant absolute angular momentum. On the other quadrants, however, the contour surfaces of  $\theta_e$  are not parallel to those of the absolute angular momentum.

Figure 9 shows the vertical cross section of mixing ratios of snow and cloud, potential temperature, vertical vorticity, and vertical velocity along the line CD in Fig. 8a. The distributions of the mixing ratios of snow  $q_s$  (Fig. 9a) and cloud  $q_c$  (Fig. 9b) show the existence of the eye almost free of snow and cloud. The surface polar low center identified as the pressure minimum is indicated by an arrow. In the eye area, a sharp lowering of the contour lines of potential temperature  $\theta$  is found (Fig. 9c), showing a warm core structure. It is also shown that at this mature stage of the polar low, its

vorticity is almost concentrated below 2000 m and is largest around 250 m above sea level (Fig. 9c). There are two regions of large vorticity on the northern and southern sides of the eye that are about 50 km apart. They correspond to the spiral cloud bands. The maximum vorticity on the southern side reaches  $4.5 \times 10^{-3} \text{ s}^{-1}$ . The axis of the vorticity tilts outward with increasing height as was reported by Yanase et al. (2002).

The distribution of the vertical velocity  $w$  shows that the central part of the eye is associated with a significant downdraft with the maximum value of  $-0.6 \text{ m s}^{-1}$ , while on the southern side of the eye, an updraft with the maximum value of  $0.9 \text{ m s}^{-1}$  is found (Fig. 9d). The maximum updraft in the northern spiral band from  $40.2^\circ$  to  $40.4^\circ\text{N}$  reaches  $2.1 \text{ m s}^{-1}$ .

### 3) THERMODYNAMIC ANALYSIS OF THE WARM CORE IN THE EYE

In order to examine the eye structure more in detail, the region between C' and D' in Fig. 9 is enlarged. Figure 10a shows the vertical cross section of mixing ratio of water vapor  $q_v$  and potential temperature  $\theta$ . The eye area at 500 m above sea level is about  $3^\circ\text{--}4^\circ\text{C}$  warmer than the environment, and it is also accompanied by a "dry core" around the height of 2000–3000 m. In order to investigate how the warm core is formed, a thermodynamic budget analysis is performed. Figures 10b, 10c, and 10d show the diabatic heating  $dQ/dt$ , the horizontal advection term  $-\mathbf{V}_h \cdot \nabla\theta$ , and the vertical advection term  $-w\partial\theta/\partial z$ , respectively, together with the potential temperature  $\theta$ . It is found that in the eye area, the contribution of diabatic heating  $dQ/dt$  is less than  $1 \text{ K h}^{-1}$  (Fig. 10b). The contribution of the horizontal advection  $-\mathbf{V}_h \cdot \nabla\theta$  changes sign along the line connecting the maximum positive potential temperature anomaly (Fig. 10c), which indicates that the main contribution of this term is to shift the potential temperature pattern toward the moving direction of the polar low. It does not contribute to an increase of the potential temperature anomaly. The contribution of the vertical advection associated with the downdraft is positive and larger than  $1 \text{ K h}^{-1}$  (Fig. 10d). Thus, it is concluded that the warm-core structure in the potential temperature is mainly caused by the downward transport of the high potential temperature air (i.e., adiabatic warming in terms of the temperature field); that is, the formation mechanism of the warm core of the polar low is similar to that found in tropical cyclones (Anthes 1982, p. 30; Yamasaki 1982, p. 171). Because of the large asymmetry in the polar low, however, the downdraft is not axisymmetric and most of the downdraft that comes into the vortex center appears to be from the east direction (cf. Yanase et al. 2002).

### 4) TIME EVOLUTION OF AREA-MEAN VARIABLES AROUND THE LOW

Figure 11 shows the hourly vertical profiles of the area-mean condensational diabatic heating rate  $dQ/dt$ ,

vertical velocity  $\bar{w}$ , moisture flux divergence  $\bar{M} = \partial(uq_v)/\partial x + \partial(vq_v)/\partial y$ , and circulation  $\bar{C}$  from 1400 to 1900 UTC, where the average is taken over a  $50 \text{ km} \times 50 \text{ km}$  square area placed around the center of the simulated surface low, and  $\bar{C} \equiv \oint \mathbf{V} \cdot d\mathbf{s}$  is calculated by a line integral along the four sides of the square area around the polar low.<sup>3</sup> The diabatic heating rate (Fig. 11a) at the earlier stage is not very large. As the time elapses, however,  $dQ/dt$  increases sharply from  $0.8 \text{ K h}^{-1}$  at 1400 UTC to  $1.8 \text{ K h}^{-1}$  at 1500 UTC. It suggests that a large amount of latent heat has been released during that period of time. At 1600 UTC, the diabatic heating rate at every level reaches its peak. The maximum heating rate appears around the height of 1500 m. At 1700 UTC, the magnitude of the diabatic heating decreases slightly but still retains its relatively large value. It should be noted that during that period of time, the diabatic heating due to the latent heat release only occurs below 5000 m, and their maximum values appear between 1000 and 2000 m (also see Fig. 9b); that is, the height of the latent heat release within the polar low is much lower than that of a hurricane/typhoon.

The vertical distribution of  $\bar{w}$ , the area-mean vertical velocity (Fig. 11b), is fairly similar to that of  $dQ/dt$ , implying that the diabatic heating is nearly compensated by the adiabatic cooling in the central area of the polar low. The maximum area-mean updraft is located at around 1500 m and is between  $0.2\text{--}0.3 \text{ m s}^{-1}$  (cf. Fig. 9d).

Figure 11c shows the area-mean divergence of the moisture flux  $\bar{M}$ . It is seen that the moisture convergence is confined to the lower 1500 m near the surface, while weak divergence exists above this height. At 1400 UTC, the convergence is weak ( $0.25 \times 10^{-6} \text{ kg kg}^{-1} \text{ s}^{-1}$ ) near the surface. It remains weak until 1500 UTC but increases to  $0.80 \times 10^{-6} \text{ kg kg}^{-1} \text{ s}^{-1}$  by 1600 UTC and maintains similar magnitude.

Figure 11d shows the area-mean circulation  $\bar{C}$ . At 1400 UTC,  $\bar{C}$  has the maximum value  $1.4 \times 10^6 \text{ m}^2 \text{ s}^{-1}$  near the surface. It remains small near the surface until 1500 UTC. After this time, however, the circulation, in association with the intensification of the area-mean vertical velocity, starts to increase at all levels continuously until 1900 UTC.

Though  $dQ/dt$  and  $\bar{w}$  start to increase at 1500 UTC,  $\bar{C}$  and  $\bar{M}$  start to increase 1 h later. This appears to indicate that the frictional convergence in the boundary layer does not become effective until the vortex reaches certain strength (e.g., Yamasaki 1983). It is also noted that the circulation increases even after the diabatic heating  $dQ/dt$  and the vertical velocity  $\bar{w}$  start to decrease after 1600 UTC. As far as the vertical velocity  $\bar{w}$  causes an inflow of air having a larger circulation from the side

<sup>3</sup> Similar calculations using different sizes of square area are found to give qualitatively similar results.

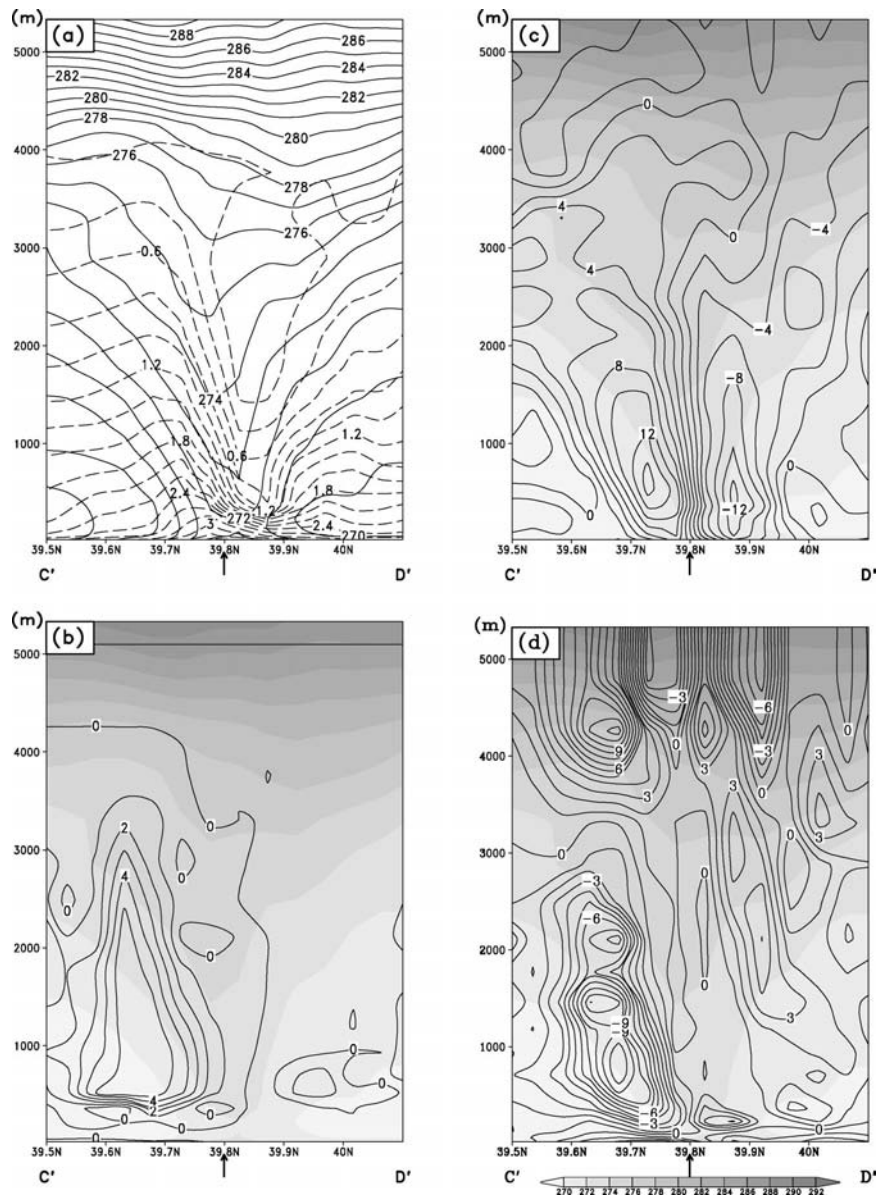


FIG. 10. Vertical cross section along the line with enlarged interval (C'D') in Fig. 9. (a) mixing ratio of water vapor  $q_v$  (dashed line;  $\text{kg kg}^{-1}$ ) and  $\theta$  (solid line; K), (b) diabatic heating (solid line;  $\text{K h}^{-1}$ ) and  $\theta$  (shaded; K), (c) horizontal advection  $-\mathbf{V}_h \cdot \nabla \theta$  (solid line;  $\text{K h}^{-1}$ ) and  $\theta$  (shaded; K), and (d) vertical advection  $-w \partial \theta / \partial z$  (solid line;  $\text{K h}^{-1}$ ) and  $\theta$  (shaded; K). The surface low center is indicated by an arrow. Note that the contour interval for (b) is  $2 \text{ K h}^{-1}$  and that for (c) and (d) is  $1 \text{ K h}^{-1}$ .

boundaries, the area-mean circulation can increase with time. The results presented in Fig. 11 show that the condensational heating is important for the vortex development, and the mechanism for the development is not inconsistent with the concept of the CISK mechanism (Ooyama 1964; Charney and Eliassen 1964). Further examinations of the mechanism for the development of the present polar low are done through sensitivity experiments in the next section.

#### 4. Sensitivity experiments

##### a. Design of the experiments

The model used for the sensitivity experiments is same as that used in section 3 except that the size of the calculation domain is  $600 \text{ km} \times 600 \text{ km}$  in the horizontal (Fig. 12) and the horizontal grid interval is  $6 \text{ km}$  to save computer resources. The time integration started from 0000 UTC 21 January 1997 and continued

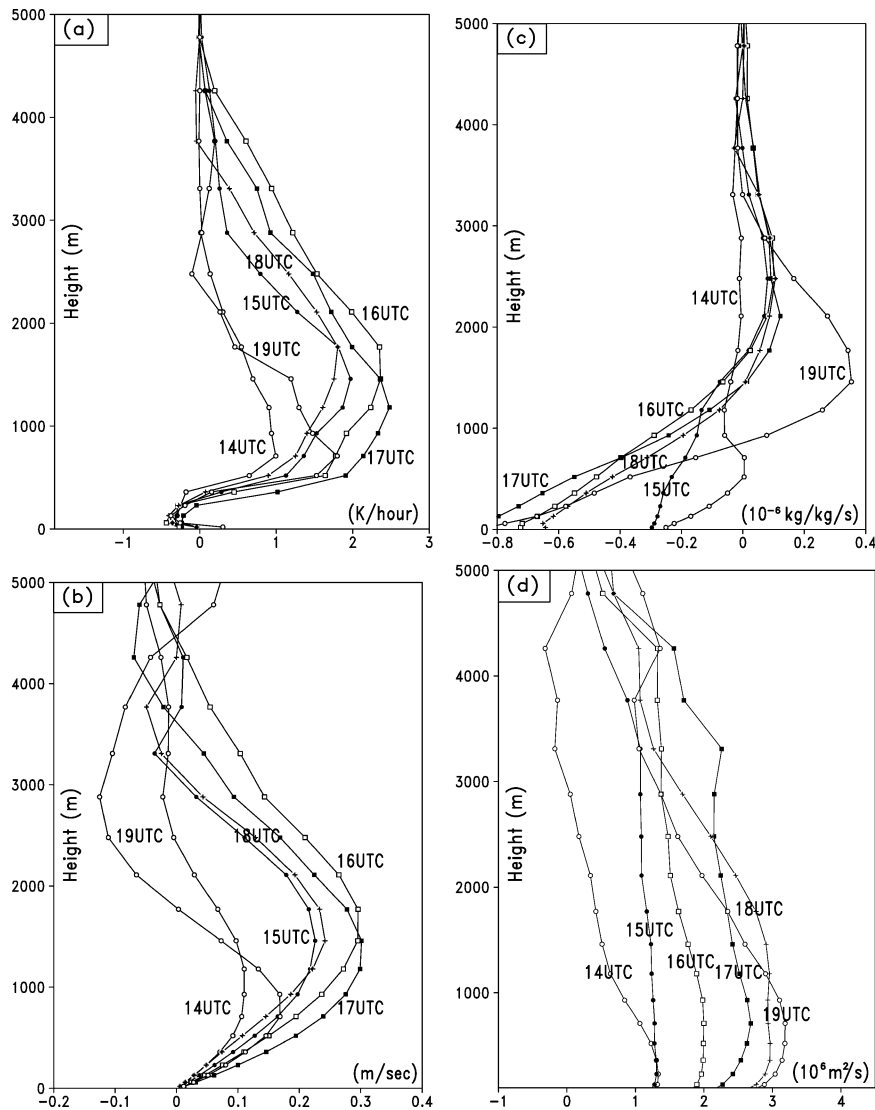


FIG. 11. Vertical profiles of area means of (a) condensational heating rate  $\overline{dQ/dt}$  ( $K h^{-1}$ ), (b) vertical velocity  $\overline{w}$  ( $m s^{-1}$ ), (c) horizontal moisture divergence  $\overline{M}$  ( $10^{-6} kg kg^{-1} s^{-1}$ ), and (d) circulation  $\overline{C}$  ( $10^6 m^2 s^{-1}$ ), at  $t = 1400, 1500, 1600, 1700, 1800,$  and  $1900$  UTC.

for 24 h. The initial and boundary conditions for MRI-NHM are taken from the 24-h prediction of RSM starting from 0000 UTC 21 January. Thus, they are the same for all of the sensitivity experiments. As will be shown later, reducing the horizontal resolution by 1 km exerts little influence on the simulated polar low development.

In the present study, the sensitivities of the polar low development to condensational heating, surface sensible heat flux, and surface latent heat flux are examined. By switching on-off these three physical processes, we have performed six experiments (CSL, XSL, CXL, CSX, CXX, and XXX) as shown in Table 3. Each experiment has a name consisting of three characters: (i) The first character is related to the condensational heating. If it is C(X), the condensational heating is switched on (off). (ii) Similarly, if the second character is S(X),

sensible heat flux is switched on (off). (iii) If the third character is L(X), latent heat flux is switched on (off). For example, CSL is the control experiment in which the full physical processes are considered, and XSL is the dry experiment without condensational heating. Although we could in principle consider eight experiments, XSX and XXL are essentially the same as XSL and XXX, respectively, so that only six experiments in Table 3 have been performed.

Two types of sensitivity experiments have been designed. One is an ordinary type in which the physical processes are switched on-off throughout the whole integration time of 24 h. The other is a new type in which the physical processes are switched on-off at a certain time during the time integration, and then the time evolution of the low is examined for an hour. In the latter

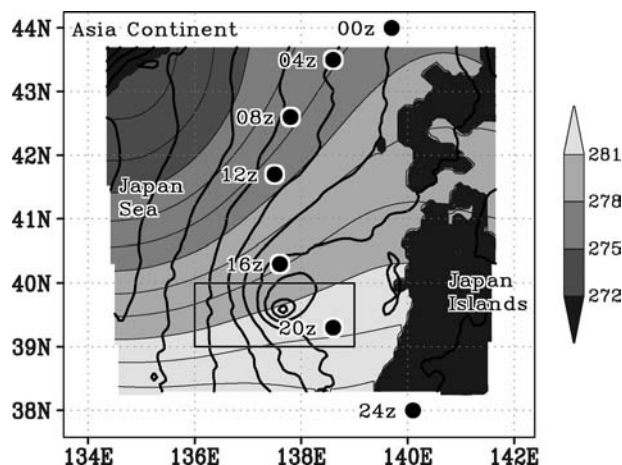


FIG. 12. The model domain for the sensitivity experiment together with the surface temperature (shaded; K) and the sea level pressure (contour interval is 2 hPa) at 1700 UTC in CSL. The pressure center of the polar low exists at 39.5°N, 137.3°E. The movement of the observed polar low is indicated by circles every 4 h from 0000 UTC. The rectangle shows the environmental area of the polar low at 1200 UTC discussed in section 5.

experiment, we expect that the deformation of the environment remains relatively small. The former will hereafter be referred to as “24-h experiment” and the latter as “1-h experiment.”

*b. Results*

1) 24-H EXPERIMENT

Figure 13 shows the time evolution of the maximum vertical vorticity in the polar low between 1200 and 1800 UTC for the 24-h experiments, where the vorticity is smoothed by taking a two-grid running mean in the horizontal directions and by averaging vertically between the surface and 1-km height in order to remove the fluctuations due to small-scale disturbances. After 1200 UTC, the polar low in CSL becomes well organized. In CSL the maximum vorticity shows that the polar low experiences a developing stage between 1200 and 1600 UTC, a mature stage between 1600 and 1700 UTC, and a dissipating stage after 1700 UTC. The polar low eventually goes out of the calculation domain after 1800 UTC.

The vorticity in CSL is the largest among the six experiments. On the contrary, it is small in CXX and XXX and remains less than  $5.0 \times 10^{-4} \text{ s}^{-1}$ . This seems to demonstrate that the surface heat fluxes are important for the polar low’s development. On the other hand, the vorticity in XSL, in which condensational heating is removed, develops moderately, with its maximum value reaching  $17.9 \times 10^{-4} \text{ s}^{-1}$  at 1700 UTC. This result suggests that the condensational heating is important to some extent but not crucially. In CXL and CSX, the vorticity becomes larger than that in XSL, but it is less than that in CSL. If one looks more in detail, one notes

TABLE 3. The setting and naming of the six sensitivity experiments.

Expt	Physical processes considered
CSL	Control run with all the physical processes included
XSL	No condensational heating
CXL	No surface sensible heat flux
CSX	No surface latent heat flux
CXX	No surface heat fluxes
XXX	No condensational heating and no surface heat fluxes

that the vorticity in CXL is larger than that in CSX until 1600 UTC, but the latter becomes larger than the former after 1700 UTC. We discuss the difference between the effects of surface sensible and latent heat fluxes on vortex development in section 5.

Since the development of the polar low is found to depend largely on the surface heat fluxes, we compare the magnitude of the surface heat fluxes for four experiments in which the surface heat flux is incorporated. In the present model, sensible (latent) heat flux is determined by the bulk method (see Table 2), so that it depends on the surface wind speed and the difference of the temperature (mixing ratio) between the sea surface and the lowest grid point (20 m above sea level). Figure 14 shows the time evolution of the area-mean surface sensible or latent heat fluxes averaged over the square region of 120 km by 120 km around the polar low center between 1200 and 1800 UTC. In CSL, the sensible (latent) heat flux increases from  $170 \text{ W m}^{-2}$  ( $160 \text{ W m}^{-2}$ ) at 1200 UTC to  $230 \text{ W m}^{-2}$  ( $220 \text{ W m}^{-2}$ ) at 1700 UTC. Although the vortex starts to dissipate at 1800 UTC, the surface heat fluxes decrease little at this time. The Bowen ratio (the ratio of sensible heat flux to the latent heat flux) is less than 1.1. The sum of the area-mean surface sensible and latent heat fluxes is 450

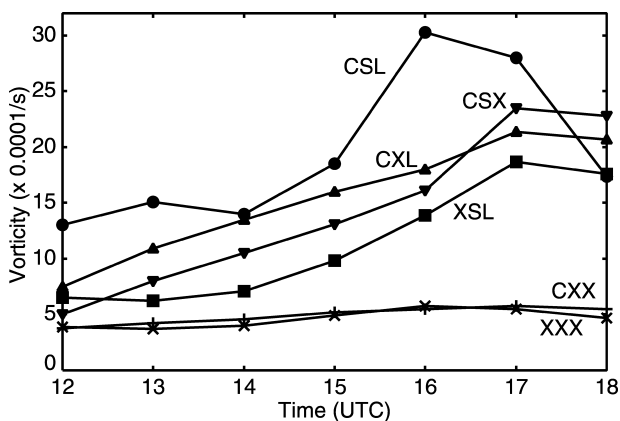


FIG. 13. Time evolutions of the maximum vorticity for the 24-h sensitivity experiments. In order to remove the fluctuations due to small-scale disturbances, the vorticity has been smoothed by taking a running mean over two grid points in each horizontal direction and averaged vertically between the surface and 1-km height. Between 1200 and 1800 UTC, the polar low in CSL is well organized. After 1800 UTC the polar low starts to dissipate and goes out of the calculation domain.

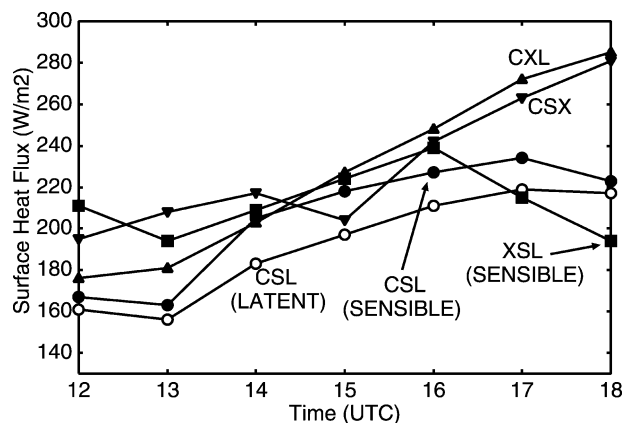


FIG. 14. Time evolutions of the surface sensible and/or latent heat fluxes around the low center for the 24-h experiments. The fluxes are averages over the 120 km × 120 km square area around the vorticity maximum.

W m<sup>-2</sup> at 1700 UTC, which is much larger than any other experiment.

The sensible heat flux is larger in CSX than that in CSL, although the vorticity in the former is less than that in the latter. As will be seen later in Fig. 16, the temperature of the low-level atmosphere in CSX turns out to be lower than that in CSL. Therefore, the temperature difference between the sea surface and the low-level atmosphere in CSX is larger than that in CSL. Similarly, the larger latent heat flux in CXL than in CSL is explained by the larger difference of mixing ratio between the sea surface and the low-level atmosphere in CXL. The sensible heat flux in CSX after 1500 UTC nearly coincides with the latent heat flux in CXL.

Now, let us look at the structure of the polar low at its mature stage in each experiment. Figure 15 shows the vertical vorticity averaged between the heights of 0 and 1 km at 1700 UTC. In CSL (Fig. 15a), the maximum vorticity of more than  $2 \times 10^{-3} \text{ s}^{-1}$  is seen at 39.5°N, 137.7°E. A band of large vorticity, which corresponds to the convergence line (Part I), extends from the vorticity maximum to the northeast. In XSL (Fig. 15b), a band of large vorticity extends from the southwest to the northeast, but no dominant vorticity maximum is seen. In CXL and CSX (Figs. 15c,d), the vorticity distribution resembles that in CSL: there is a clear vorticity maximum, and the vorticity band extends northeastward from the maximum. In CXX and XXX (Figs. 15e,f), both the vorticity maximum and the vorticity band are much weaker. The vorticity remains only about  $5 \times 10^{-4} \text{ s}^{-1}$  in these experiments.

Also shown in Fig. 15 are potential temperature distributions at  $z = 4260 \text{ m}$ . Experiments XSL and XXX (Figs. 15b,f) show nearly similar distributions of the potential temperature associated with the cold vortex (cf. Fig. 2c of Part I); that is, the distributions of the potential temperature in XSL and XXX are little modified by cumulus convections originating from the top

of the convective boundary layer. In experiments with condensational heating (Figs. 15a, 15c, 15d, and 15e), on the other hand, the northeastern part of the cold air seems to be eroded because of condensational heating associated with the cumulus convections. This erosion is most significant for CSL. Thus, the approach of the upper-level cold vortex and associated destabilization of the stratification seems to have played some role in the development of the present low.

Figure 16 shows the zonal-vertical cross sections of the vertical vorticity and potential temperature through the low center at 1700 UTC. In CSL (Fig. 16a), the low center is located at 137.7°E (see Fig. 15a). The vorticity is largest below 1.5 km AGL and reaches more than  $2 \times 10^{-3} \text{ s}^{-1}$ . The vorticity contour line of  $5 \times 10^{-4} \text{ s}^{-1}$  extends to the height of about 5.5 km. The potential temperature has a large vertical gradient above the height of about 5 km, showing that the tropopause is lowered because of the presence of the cold vortex (Part I). A warm-core structure near the low center is clearly seen below the height of 5 km.

In XSL (Fig. 16b), a region of large vorticity exceeding  $1 \times 10^{-4} \text{ s}^{-1}$  exists only below the height of 1.5 km. To the west of the low center, between 136° and 138°E, the potential temperature between the heights of 2 and 4 km is lower than that in CSL because of a removal of the condensational heating. In CXX and XXX (Figs. 16e,f), a region with vorticity larger than  $5 \times 10^{-4} \text{ s}^{-1}$  exists only below 1 km AGL, where the atmosphere is strongly stratified because of the absence of surface heat fluxes. It is noted that another region of large vorticity is seen above 3 km AGL between 136° and 138°E. This is thought to be associated with the upper-level cold vortex. In CXL and CSX (Figs. 16c,d), the structure of the low much resembles that in CSL: a region with vorticity larger than  $1 \times 10^{-3} \text{ s}^{-1}$  extends to about 4.5 km AGL, and that larger than  $2 \times 10^{-3} \text{ s}^{-1}$  exists below 1 km AGL. The warm-core structure below 1 km AGL in CSX, however, is much clearer than in CXL.

## 2) 1-H EXPERIMENT

Figure 17 shows the time evolution of the maximum vertical vorticity for the 1-h experiments. The result for CSL is the same as that in the 24-h experiments. For the other sensitivity experiments, CSL is run until  $n$  UTC, where  $n$  is an integer between 11 and 17, and then the sensitivity runs are made for an hour by switching off particular physical processes. In the figure, the resulting vorticity at  $(n + 1)$  UTC is plotted for each sensitivity run. The weakest vorticity development occurs for XSL and XXX, for which condensational heating is switched off. To the contrary, strong development comparable to that for CSL occurs for CXL, CSX, and CXX. These results show that the condensational heating is essential for the vortex development, but the surface heat fluxes are hardly important on the time scale

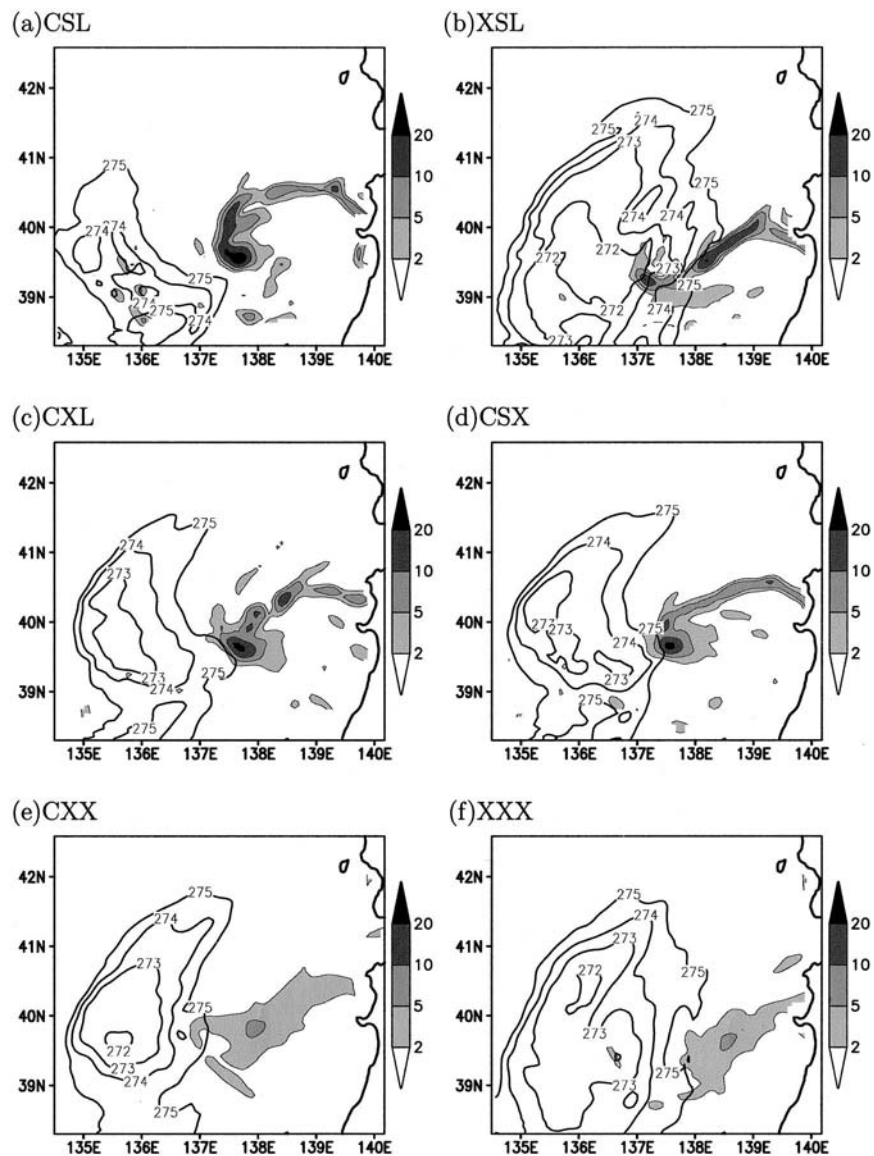


FIG. 15. The vorticity averaged vertically between 0 and 1 km (grayscale,  $10^{-4} \text{ s}^{-1}$ ), and potential temperature at  $z = 4260 \text{ m}$  (thin solid contour line drawn for each 1 K below 275 K) at 1700 UTC for each sensitivity experiment. The vorticity is shown only over the sea.

of 1 h, which seems to be in apparent contradiction to the results for the 24-h experiments. This point is discussed in section 5b.

## 5. Discussion

### a. Comparison with the previous sensitivity studies

First, we briefly compare the results of the present sensitivity experiments with those of the previous sensitivity studies. Since physical processes are switched off throughout the lifetime of the polar low (more than 24 h) in almost all the previous sensitivity studies, it

would be appropriate to compare their results with those of our 24-h experiment (Fig. 13).

In the present 24-h experiment, the most important physical processes appear to be the surface heat fluxes because the polar low hardly develops in their absence, as seen in CXX. In most of the previous studies such as the Atlantic case in Sardie and Warner (1985), the Hudson Bay case in Albright and Reed (1995), the Bering Sea case in Bresch et al. (1997), and the Japan Sea case in Lee et al. (1998), polar lows failed to develop in the absence of the surface heat fluxes. It is discussed in the following sections how surface heat fluxes affect the polar low development. The only exception is the

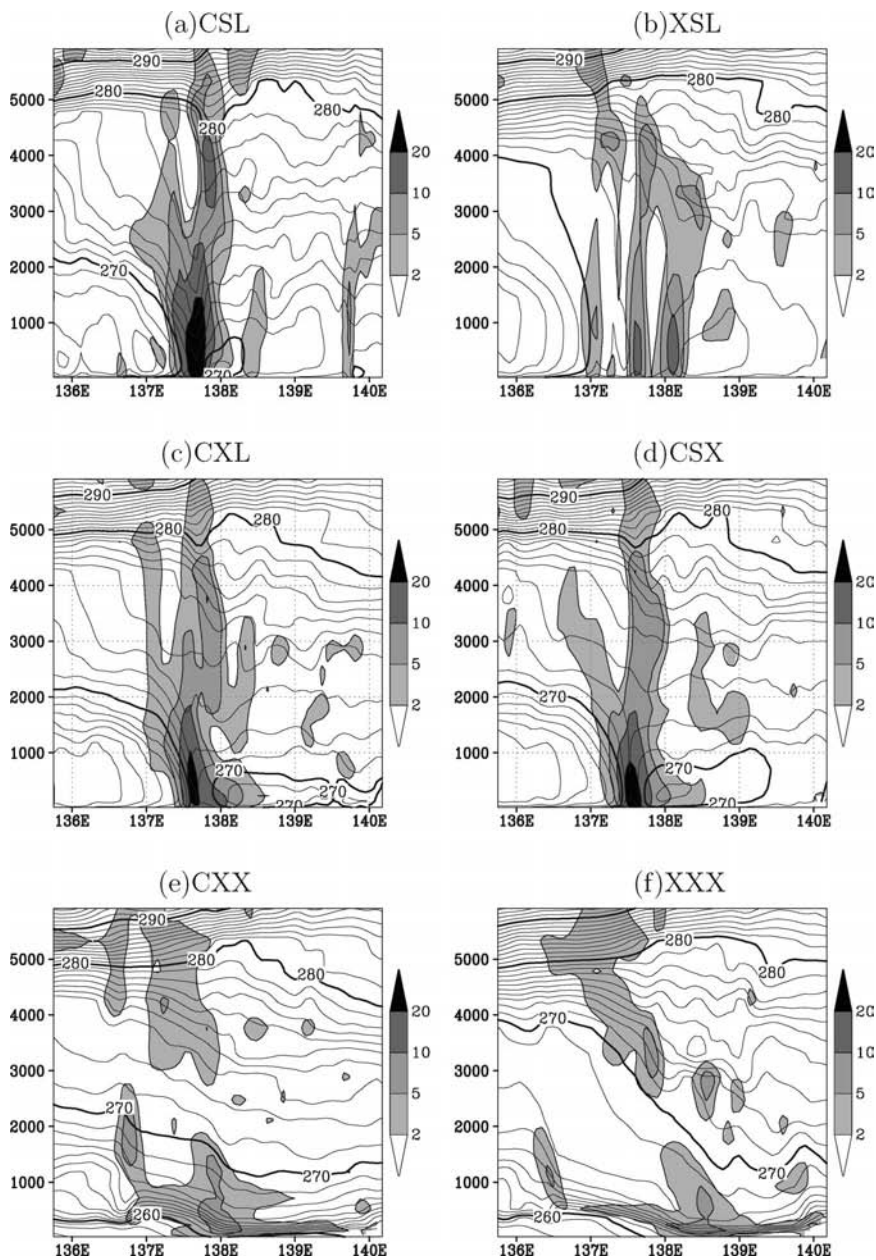


FIG. 16. The vorticity (grayscale,  $10^{-4} \text{ s}^{-1}$ ) and potential temperature (thin and thick contour intervals are 1 and 10 K, respectively) on the zonal-vertical cross section through each simulated low center at 1700 UTC. The latitudes of the cross sections are as follows: (a) CSL, 39.5°N; (b) XSL, 39.4°N; (c) CXL, 39.7°N; (d) CSX, 39.7°N; (e) CXX, 39.8°N; and (f) XXX, 39.5°N.

Pacific case in Sardie and Warner (1985) for which a deep baroclinity rather than the surface fluxes was important for the polar low development.

The condensational heating, on the other hand, appears to be important to some extent but not crucially in the present 24-h experiment because the polar low developed only moderately in XSL. In Bresch et al. (1997), the polar low also develops only moderately in the absence of the condensational heating, whereas in

other studies [e.g., the Atlantic case of Sardie and Warner (1985); Albright and Reed (1995)] the polar lows failed to develop.

Thus, the present results for 24-h experiment can be said to be similar to those of the previous studies with respect to the effect of the surface heat fluxes. The effect of the condensational heating, however, seems to vary from case to case, so that it is not easy to discuss how typical the present result is.

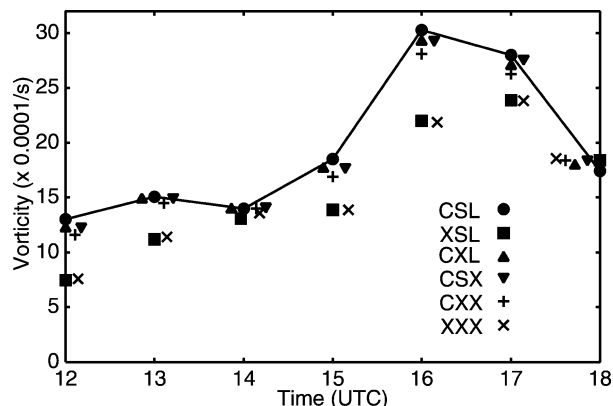


FIG. 17. Time evolutions of the maximum vorticity for the 1-h sensitivity experiments. The vorticity for the sensitivity experiment at 1300 UTC, for example, is obtained by running CSL until 1200 UTC and then switching on-off the physical processes for 1 h.

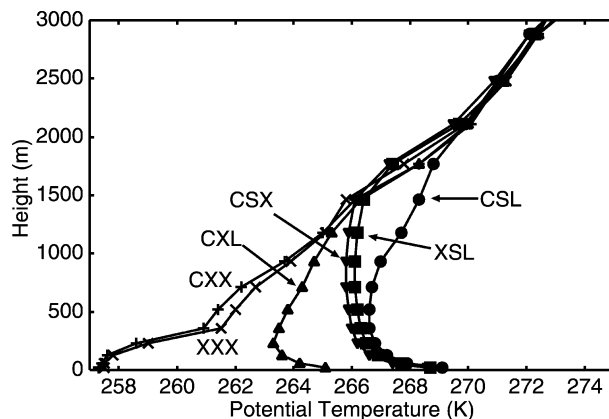


FIG. 18. The vertical profiles of the potential temperature in the environmental atmosphere for the 24-h experiments. The potential temperature is averaged over the area to the south of the polar low (39°–40°N, 136°–139°E) at 1200 UTC, which is not yet affected by the polar low.

*b. Problem in the ordinary sensitivity experiments and its remedy*

As has been pointed out in the introduction, the commonly performed sensitivity experiment like the 24-h experiment in the present study has the problem that a removal of a certain physical process for a long time deforms not only the vortex itself but also the environment in which the vortex develops. Figure 18 shows the vertical profiles of the average potential temperature over the environmental area at 1200 UTC, where the environmental area is defined by the rectangular area of 39°–40°N, 136°–139°E (see Fig. 12). Note that this area is located far to the south of the polar low at 1200 UTC, but the polar low eventually passes over the area. The vertical profiles of the environmental potential temperature show significant variations among the experiments and may be classified into four groups: (i) In CSL, the potential temperature at the low level is highest among the six experiments. A convective mixed layer develops to the height of 2.5 km. It consists of two parts: a dry mixed layer below 700 m and a moist mixed layer above. Such a two-layer structure is consistent with the previous numerical simulation of the moist convective mixed layer (e.g., Asai and Nakamura 1978). (ii) Experiments CSX and XSL behave nearly in a similar manner: a dry mixed layer with constant potential temperature of 266 K is seen below the height of 1.5 km. (iii) In CXL, the moist mixed layer exists below the height of 1.2 km. The potential temperature at the low level is considerably lower than that for CSX and XSL. (iv) In CXX and XXX, the surface potential temperature is very low. The lower atmosphere is very stably stratified because of the absence of the surface heat fluxes. Given such differences in the environmental potential temperature, it is not possible to clarify which caused the development mechanisms of the polar low: the modified environment or the physical processes directly acting on the vortex. This is why we have performed the

1-h experiment, in which we hoped that the environment of the vortex deforms little and the effect of the physical process on the vortex itself would be clarified.

In the 1-h experiment, the condensational heating turned out to be very important for the polar low development whereas the surface heat fluxes are found to be of little importance (Fig. 17). This result appears to conflict with that in the 24-h experiments in which the surface heat fluxes are primarily important and the condensational heating is of secondary importance. This apparent paradox may be interpreted as follows: In the 1-h experiment, the absence of the surface heat fluxes for such a short time hardly deforms the environmental atmosphere. In fact, the vertical profile of the environmental potential temperature for each run turned out to be similar to that for CSL (not shown). In CSL, CXL, CSX, and CXX, the vortex develops by condensating the water vapor that is already present in the environment. In particular, this feature is most pronounced for the period between 1500 and 1600 UTC when the vortex develops most rapidly. In XSL and XXX, on the other hand, the vortex fails to develop in the absence of the condensational heating.

Now, the results of both 24- and 1-h experiments lead us to two important conclusions: First, given the environment of CSL, the condensational heating is the most important physical process that directly causes the rapid vortex development as seen in the 1-h experiment. Second, the surface heat fluxes are important in the sense that they affect the vortex development indirectly through the modification of the environment, as seen in the 24-h experiment.

An additional sensitivity experiment has been made to reinforce our conclusions described above. In this experiment, which will be referred to as the “6-h experiment,” CSL is run until 1200 UTC and then a time integration is continued by switching on-off particular physical processes until 1800 UTC. Figure 19 shows

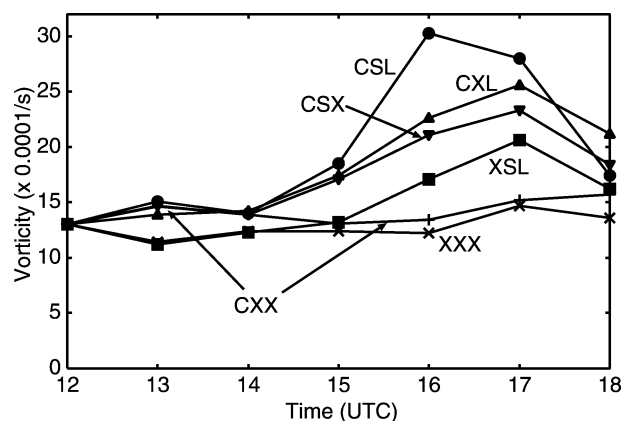


FIG. 19. Time evolutions of the maximum vorticity for the 6-h sensitivity experiments in which CSL is run until 1200 UTC, and then the physical processes are switched on-off for 6 h.

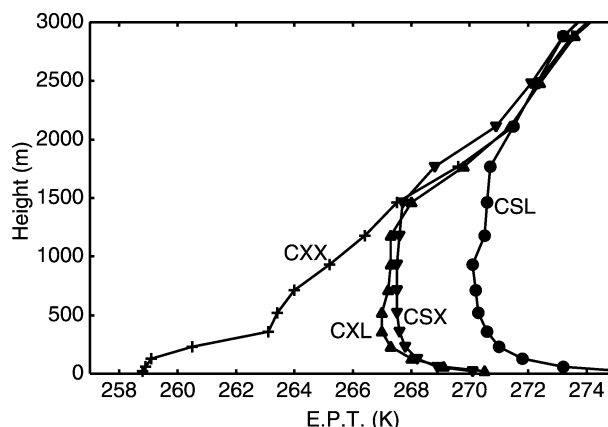


FIG. 20. Same as Fig. 18 except for the equivalent potential temperature and for CSL, CSX, CXL, and CXX.

the resulting time evolution of the vorticity for each experiment. During the first 2 h, the vorticity in CXX evolves similarly to that in CSL. After 1400 UTC, however, the absence of the surface heat fluxes starts to affect the vortex development and the growth of the vorticity in CXX becomes weaker than that in CSL. Thus, a removal of surface heat fluxes seems to affect the vortex environment after a few hours.

*c. Development mechanism of the polar low*

The previous studies have suggested a number of development mechanisms of the polar low such as baroclinic instability (Mansfield 1974; Reed and Duncan 1987), CISK (Rasmussen 1979; Bratseth 1985), WISHE (Emanuel and Rotunno 1989), and influence of an upper-level mobile trough (Montgomery and Farrell 1992; Grønås and Kvamstø 1995). These mechanisms seem to operate with different importance depending on regions, cases, and stages. Thus, it is not an easy task to understand the development mechanism of the polar low. The results of the present numerical simulation with full physics and with the sensitivity experiments give us some understanding of the development mechanism of the polar low. In the following, we are not concerned with the initial perturbation that triggered the polar low, because we are not confident that the detailed structure of the initial perturbation is resolved by the RSM, which gives the initial and boundary condition for MRI-NHM.

Baroclinic instability has been one of the possible candidates for the development mechanism of the polar low, because some baroclinity almost always exists in the environment where polar lows develop. The fact that the vortex develops moderately in XSL in the 24-h experiment (Fig. 2), in which moist processes are excluded, suggests that the dry baroclinic process seems to be operating to some extent for the present polar low development. Several features of the result in the 24-h

experiment, however, are not satisfactorily explained only by the dry baroclinic process: First, the growth rate calculated from the evolution of the simulated vorticity in CSL in the 24-h experiment is larger than that estimated from the linear instability study of the Eady (1949) model. While the growth rate of the simulated vortex in CSL in the 24-h experiment is as large as  $3.2 \times 10^{-5} \text{ s}^{-1}$  from 1200 to 1500 UTC and even attains  $1.4 \times 10^{-4} \text{ s}^{-1}$  from 1500 to 1600 UTC, that estimated from the linear instability study is at most  $2 \times 10^{-5} \text{ s}^{-1}$ , where a Brunt-Väisälä frequency of  $8.3 \times 10^{-3} \text{ s}^{-1}$  and vertical wind shear of about  $5 \times 10^{-3} \text{ s}^{-1}$  are assumed.

Second, it is curious that the polar low development in CXL is nearly similar to that in CSX in the 24-h experiment, although the low-level atmosphere in CXL is much more stable than that in CSX (see Fig. 18). These two points may be resolved when one considers the effect of condensational heating. Figure 20 shows the vertical profiles of equivalent potential temperature for the 24-h experiments. The vertical profiles of the equivalent potential temperature in CSL and CXL have less vertical gradient than those of the potential temperature. The high equivalent potential temperature at low level is due to a large amount of water vapor. If the vertical motion in the polar low is accompanied by “large scale” condensation, and therefore the static stability is effectively reduced, the growth rate theoretically estimated from the linear instability study may explain the large growth rate of simulated vorticity in CSL and CXL in the 24-h experiment (except for the large growth rate in CSL from 1500 to 1600 UTC). Thus, the dry baroclinic instability, if any, explains only partly the growth rate of about  $3 \times 10^{-5} \text{ s}^{-1}$  of the present polar low. This conclusion is similar to that of Sardie and Warner (1983), who concluded that the growth rate of dry baroclinic instability is too small to explain the observed value for each case of them.

Given the environment of CSL, the condensational heating is most important for the rapid development of

the polar low as seen in the 1-h experiment. As has been mentioned, baroclinic instability with large-scale condensation is one of the promising candidates to explain at least partly the growth rate of the simulated vortex in CSL in the 24-h experiment between 1200 and 1500 UTC. However, the extremely large growth rate of  $1.4 \times 10^{-4} \text{ s}^{-1}$  from 1500 and 1600 UTC does not seem to be explained by the baroclinic instability, because the growth rate by normal-mode baroclinic instability is at most about 30% of the Coriolis parameter (Stone 1966). Hence, other mechanisms are required. The most probable mechanism is CISK, in which cooperation between the parent vortex and cumulus convections contribute to the development of the vortex. In fact, the results in section 3 indicate that the relationships among the convergence of the water vapor at the low level, the area-mean vertical velocity, the area-mean circulation, and the area-mean condensational heating are not inconsistent with the CISK mechanism.

Montgomery and Farrell (1992) suggested that when an upper-level trough approaches the low-level polar low it could diabatically destabilize the atmosphere and increase the low-level potential vorticity. In the present case, an upper-level cold vortex did come over the polar low at the mature stage (see Figs. 2a,c of Part I), which is well simulated in each sensitivity experiment (Fig. 15). As was described in section 4b(1), the diabatic destabilization by the upper-level trough seems to have played some role in the vortex development.

Emanuel and Rotunno (1989, hereafter ER89) suggested another mechanism by axisymmetric model: As the vortex and associated surface wind grow stronger, surface heat fluxes act to increase the entropy at the vortex center through the horizontal transport of heat by low-level inflow and the vertical transport by cumulus convections. The associated buoyancy at the vortex center would lead to convergence at low-level atmosphere and thereby to further spinup of the vortex. The essence of this mechanism is a positive feedback between sea surface heat fluxes and surface wind of the vortex, through which the vortex intensifies. The time scale for the vortex development in ER89's numerical simulation, however, is a few tens of hours, which seems difficult to explain the large growth rate of the present polar low by itself. Furthermore, the surface heat fluxes in the present case are largely contributed by the ambient northerly flow, but little by the tangential wind of the vortex. This is well reflected in the vortex development in CSL of the 24-h experiment. Although the vortex starts to dissipate after 1600 UTC, the surface heat fluxes retain their magnitude (see Figs. 13 and 14), which is not consistent with the feedback mechanism of ER89. Thus, the present study has little support for ER89's feedback mechanism.

## 6. Summary

A remarkable isolated polar low observed over the Japan Sea on 21 January 1997 (Part I) was numerically

studied using RSM of 20-km horizontal mesh and MRI-NHM with 5-km horizontal mesh, which is one-way nested in RSM.

The 24-h prediction of RSM started from 0000 UTC 21 January reproduced quite well the polar low's position and intensity as well as the initial wrapping of the west part of the east-west-oriented vorticity zone. The vorticity budget analysis indicated that the stretching term played a dominant role in the polar low development.

A simulation by MRI-NHM reproduced surprisingly well the initial wrapping of the western part of the east-west-oriented cloud band accompanied by the shear line, the spiral-shaped cloud pattern, and the eye structure near the vortex center. The simulated polar low exhibited a large deviation from axisymmetry: The wind speed associated with the polar low was much larger in the western side of the low center than in the eastern side. Accordingly, the surface heat flux was also much larger in the western side. The eye was occupied by warm dry air associated with a strong downdraft and was almost free of cloud. The detailed thermodynamic budget analysis indicated that the warm core was mainly caused by the adiabatic warming associated with the downdraft. The vertical profiles of the area-mean condensational heating, the vertical velocity, the convergence of the moisture flux, and the circulation averaged over a  $50 \text{ km} \times 50 \text{ km}$  square area near the vortex center showed that the development mechanism of the polar low was not inconsistent with CISK.

In order to clarify the development mechanism of the polar low in more detail, sensitivity experiments were performed using a mesoscale nonhydrostatic numerical model (MRI-NHM) in which the effects of condensational heating and surface heat fluxes are switched on-off. First, an ordinary type of sensitivity study was designed, where the physical process was switched on-off throughout the whole integration time of 24 h (24-h experiment). In this experiment, the surface heat fluxes were found to be crucially important whereas the condensational heating was of secondary importance. Second, a new type of sensitivity experiment in which the physical processes were switched on-off only for 1 h was designed in order to remedy the problem of the 24-h experiment that the absence of the physical processes for a long time not only affects the vortex but also deforms the environment of the vortex significantly. In the 1-h experiment, the condensational heating turned out to be most important whereas the surface heat fluxes hardly affected the vortex development.

These two types of sensitivity experiments revealed the following: The condensational heating is of primary importance for the rapid intensification of the present polar low. Thus, dry processes such as baroclinic instability are insufficient for explaining the rapid development of the polar low. On the other hand, surface heat fluxes are important in the sense that they maintain the less stable stratification of the environmental at-

mosphere and are thus favorable for the vortex development.

*Acknowledgments.* This paper is a part of WY's M.S. thesis and a part of FG's Ph.D. thesis, submitted to the Department of Earth and Planetary Physics, University of Tokyo, in March 2001 and in March 1999, respectively. The authors are grateful to Prof. Shang-Ping Xie, Prof. G. W. Kent Moore, and one anonymous reviewer for their thoughtful comments that contributed to improve the quality of the manuscript significantly. Thanks are also extended to the staff and students at Dynamic Marine Meteorology Group, Ocean Research Institute, University of Tokyo, for their help and encouragement.

FG was partly supported by the Chinese Ministry of Education and the Japanese Ministry of Education, Culture, Sports, Science and Technology (MEXT) through their scholarship exchange programs and the National Nature Science Foundation of China under Grants 40275033 and 40240420564. WY was partly supported by a Grant for the 21st Century COE Program "Predictability of the Evolution and Variation of the Multi-scale Earth System: An Integrated COE for Observational and Computational Earth Science" from MEXT. This work was partly supported by Grant-in-Aid for Scientific Research on Priority Areas (B) 12125201, MEXT, and by Grant-in-Aid for Scientific Research 14340138, Japan Society for the Promotion of Science. The present simulations were done using the Meteorological Research Institute Nonhydrostatic Model (MRI-NHM). Dr. Kazuo Saito, Numerical Prediction Division of the Japan Meteorological Agency helped the authors to use the model in various aspects and is very much appreciated. The figures are prepared by the Grid Analysis and Display System (GrADS) implemented by Brian Doty.

#### REFERENCES

- Albright, M. D., and R. J. Reed, 1995: Origin and structure of a numerically simulated polar low over Hudson Bay. *Tellus*, **47A**, 834–848.
- Anthes, R. A., 1982: *Tropical Cyclones—Their Evolution, Structure, and Effects*. Meteor. Monogr., No. 41, Amer. Meteor. Soc., 208 pp.
- Asai, T., and K. Nakamura, 1978: A numerical experiment of airmass transformation processes over warmer sea. Part I: Development of a convectively mixed layer. *J. Meteor. Soc. Japan*, **56**, 424–434.
- Benwell, G. R. R., and F. H. Bushby, 1970: A case study of frontal behavior using a 10-level primitive equation model. *Quart. J. Roy. Meteor. Soc.*, **96**, 287–296.
- Bratseth, A. M., 1985: A note on CISK in polar air masses. *Tellus*, **37A**, 403–406.
- Bresch, J. F., R. J. Reed, and M. D. Albright, 1997: A polar low development over the Bering Sea: Analysis, numerical simulation, and sensitivity experiments. *Mon. Wea. Rev.*, **125**, 3109–3130.
- Charney, J. G., and A. Eliassen, 1964: On the growth of the hurricane depression. *J. Atmos. Sci.*, **21**, 68–75.
- Craig, G. C., and S. L. Gray, 1996: CISK or WISHE as the mechanism for tropical cyclone intensification. *J. Atmos. Sci.*, **53**, 3528–3540.
- Davies, H. C., 1976: A lateral boundary formulation for multi-level prediction models. *Quart. J. Roy. Meteor. Soc.*, **102**, 405–418.
- Eady, E. T., 1949: Long waves and cyclone waves. *Tellus*, **1**, 33–52.
- Emanuel, K. A., 1986: An air–sea interaction theory for tropical cyclones. Part I: Steady-state maintenance. *J. Atmos. Sci.*, **43**, 585–604.
- , and R. Rotunno, 1989: Polar lows as arctic hurricanes. *Tellus*, **41A**, 1–17.
- , J. D. Neelin, and C. S. Bretherton, 1994: On large-scale circulation in convecting atmosphere. *Quart. J. Roy. Meteor. Soc.*, **120**, 1111–1144.
- Fu, G., H. Niino, R. Kimura, and T. Kato, 2004: A polar low over the Japan Sea on 21 January 1997. Part I: Observational analysis. *Mon. Wea. Rev.*, **132**, 1537–1551.
- Gadd, A. J., and J. F. Keers, 1970: Surface exchange of sensible heat in a 10-level model atmosphere. *Quart. J. Roy. Meteor. Soc.*, **96**, 297–308.
- Gal-Chen, T., and R. C. Somerville, 1975: On the use of a coordinate transformation for the solution of the Navier–Stokes equations. *J. Comput. Phys.*, **17**, 209–228.
- Gill, A. E., 1982: *Atmospheric–Ocean Dynamics*. Academic Press, 662 pp.
- Gray, S. L., and G. C. Craig, 1998: A simple theoretical model for the intensification of tropical cyclones and polar lows. *Quart. J. Roy. Meteor. Soc.*, **124**, 919–947.
- Grønås, S., and N. G. Kvamstø, 1995: Numerical simulations of the synoptic conditions and development of arctic outbreak polar lows. *Tellus*, **47A**, 797–814.
- Harley, D. G., 1960: Frontal contour analysis of a polar low. *Meteor. Mag.*, **89**, 146–147.
- Harrold, T. W., and K. A. Browning, 1969: The polar low as a baroclinic disturbance. *Quart. J. Roy. Meteor. Soc.*, **95**, 710–723.
- Ikawa, M., and K. Saito, 1991: Description of a nonhydrostatic model developed at the Forecast Research Department of the MRI. Vol. 28, MRI Tech. Rep., 238 pp.
- Kain, J. S., and J. M. Fritsch, 1993: Convective parameterization for mesoscale models: The Kain–Fritsch scheme. *The Representation of Cumulus Convection in Numerical Models of the Atmosphere*, Meteor. Monogr., No. 46, Amer. Meteor. Soc., 165–177.
- Kato, T., 1995: A box-Lagrangian rain-drop scheme. *J. Meteor. Soc. Japan*, **73**, 241–245.
- , 1996: Hydrostatic and non-hydrostatic simulations of the 6 August 1993 Kagoshima torrential rain. *J. Meteor. Soc. Japan*, **74**, 355–363.
- Kondo, J., 1975: Air–sea bulk transfer coefficients in diabatic conditions. *Bound.-Layer Meteor.*, **9**, 91–112.
- Lee, T. Y., Y. Y. Park, and Y. L. Lin, 1998: A numerical modeling study of mesoscale cyclogenesis to the east of the Korean peninsula. *Mon. Wea. Rev.*, **126**, 2305–2329.
- Louis, J. F., M. Tiedke, and J. F. Geleyn, 1981: A short history of the operational PBL-parameterization at ECMWF. *Proc. Workshop on Planetary Boundary Layer Parameterization*, Reading, United Kingdom, ECMWF, 59–79.
- Mansfield, D. A., 1974: Polar lows: The development of baroclinic disturbances in cold air outbreaks. *Quart. J. Roy. Meteor. Soc.*, **100**, 541–554.
- Mellor, G. L., and T. Yamada, 1974: A hierarchy of turbulence closure models for planetary boundary layers. *J. Atmos. Sci.*, **31**, 1791–1806.
- Montgomery, M. T., and B. F. Farrell, 1992: Polar low dynamics. *J. Atmos. Sci.*, **49**, 2484–2505.
- Nakamura, M., 1995: Verification of the new JSM. Text for the numerical prediction, Forecast Department, Japan Meteorological Agency, Vol. 25, 10–38.
- Ogura, Y., and T. Takahashi, 1971: Numerical simulation of the life cycle of a thunderstorm cell. *Mon. Wea. Rev.*, **99**, 895–911.

- Ooyama, K., 1964: A dynamical model for the study of tropical cyclone development. *Geophys. Int.*, **4**, 187–198.
- Pagowski, M., and G. W. K. Moore, 2001: A numerical study of an extreme cold-air outbreak over the Labrador Sea: Sea ice, air-sea interaction, and development of polar lows. *Mon. Wea. Rev.*, **129**, 47–72.
- Rasmussen, E., 1979: The polar low as an extratropical CISK disturbance. *Quart. J. Roy. Meteor. Soc.*, **105**, 531–549.
- Reed, R. J., and C. N. Duncan, 1987: Baroclinic instability as a mechanism for the serial development of polar lows: A case study. *Tellus*, **39A**, 376–384.
- Saito, K., 1993: A numerical study of the local downslope wind “Yamaji-kase” in Japan. Part 2: Non-linear aspect of the 3-D flow over a mountain range with a col. *J. Meteor. Soc. Japan*, **71**, 69–91.
- , 1994: A numerical study of the local downslope wind “Yamaji-kase” in Japan. Part 3: Numerical simulation of the 1991 September wind-storm with a non-hydrostatic multi-nested model. *J. Meteor. Soc. Japan*, **72**, 301–329.
- , 1997: Semi-implicit fully compressible version of the MRI mesoscale nonhydrostatic model—Forecast experiment of the 6 August 1993 Kagoshima torrential rain. *Geophys. Mag.*, **2**, 109–137.
- , 1998: On the MRI mesoscale nonhydrostatic model (in Japanese). *Proc. Annual Meeting of the JMA for the Improvement of Forecasting Techniques*, Tokyo, Japan, MRI, 39–58.
- , and T. Kato, 1996: On the modification of the MRI nonhydrostatic nesting model (in Japanese). *Tenki*, **43**, 369–382.
- Sardie, J. M., and T. T. Warner, 1983: On the mechanism for the development of polar lows. *J. Atmos. Sci.*, **40**, 869–881.
- , and ———, 1985: A numerical study of the development mechanism of polar lows. *Tellus*, **37A**, 460–477.
- Sommeria, G., 1976: Three-dimensional simulation of turbulent processes in an undisturbed trade wind boundary layer. *J. Atmos. Sci.*, **33**, 216–241.
- Stone, P. H., 1966: On non-geostrophic baroclinic stability. *J. Atmos. Sci.*, **23**, 390–400.
- Sugi, M., K. Kuma, K. Tada, K. Tamiya, N. Hasegawa, T. Iwasaki, S. Yamada, and T. Kitade, 1990: Description and performance of the JMA operational global spectral model (JMA-GSM88). *Geophys. Mag.*, **43**, 105–130.
- Tatsumi, Y., 1986: A spectral limited-area model with time-dependent lateral boundary conditions and its application to a multi-level primitive equation model. *J. Meteor. Soc. Japan*, **64**, 637–663.
- Yamasaki, M., 1982: *Typhoon* (in Japanese). Tokyo-do Press, 206 pp.
- , 1983: A further study of the tropical cyclone without parameterizing the effects of cumulus convection. *Pap. Geophys. Meteor.*, **34**, 221–260.
- Yanase, W., H. Niino, and K. Saito, 2002: High-resolution numerical simulation of a polar low. *Geophys. Res. Lett.*, **29**, 1658, 10.1029/2002GL014736.